This is a preprint, the final version is subject to change, of the American Mineralogist (MSA)
Cite as Authors (Year) Title. American Mineralogist, in press.
(DOI will not work until issue is live.) DOI: http://dx.doi.org/10.2138/am-2015-4839

REVISION 2: Monazite, zircon, and garnet growth in migmatitic pelites as a record of metamorphism and partial melting in the East Humboldt Range, Nevada

Benjamin W. Hallett[1,*] and Frank S. Spear[1]

[1] Department of Earth and Environmental Sciences, Rensselaer Polytechnic Institute, Troy, New York 12180, U.S.A.

* Present address: Department of Geology, University of Wisconsin Oshkosh, Oshkosh, Wisconsin 54901, U.S.A., E-mail: hallettb@uwosh.edu, phone: 920-424-0868, fax: 920-424-0240

ABSTRACT

Monazite and zircon thermometry and geochronology were applied to anatectic pelites of the northern East Humboldt Range, Nevada. The study area is an exhumed portion of the Sevier orogenic root and is characterized by two crustal blocks with different prograde metamorphic histories: the Winchell Lake nappe and the underlying Lizzies Basin block. U/Th–Pb Secondary Ion Mass Spectrometry (SHRIMP) results from zircon and monazite indicate that in the Lizzies Basin block prograde metamorphism began by 96.5 ± 8.0 Ma. Cooling and melt crystallization was initiated by 80.1 ± 1.4 Ma. Possible reheating and a monazite growth event occurred again at 76.2 ± 2.8 to 68.2 ± 2.0 Ma. In the upper limb of the overlying Winchell Lake nappe, prograde metamorphism began by 82.8 ± 1.3 Ma. Cooling and melt crystallization recorded by zircon and monazite growth/recrystallization at 77.4 ± 12.4 to 58.9 ± 3.6 Ma. Melt may have been present in the Winchell Lake nappe upper limb for a protracted period, or may have formed during several

unresolved melting events. Thin Eocene–Oligocene (~40–32 Ma) high Y monazite rims are found in both crustal blocks. These probably represent a phase of heating during Eocene–Oligocene magmatism and extensional deformation. U/Th–Pb geochronology results are consistent with differential burial, heating, and exhumation of different crustal blocks within the East Humboldt Range. Significantly fast exhumation of upper limb rocks of the Winchell Lake nappe and somewhat slower exhumation of Lizzies Basin block rock occurred prior to the "core complex" phase of the exhumation of the Ruby Mountains–East Humboldt Range metamorphic core complex. Differences in the timing and tectonic significance of exhumation episodes within the East Humboldt Range may indicate how the localized presence of partial melt can affect the evolution of an exhumed orogenic terrane.

Keywords: SHRIMP, monazite, metamorphic core complex, trace elements, migmatite, exhumation

INTRODUCTION

The significance of partial melting (anatexis) related to regional metamorphism in the exhumed roots of ancient mountain belts is a major focus of recent petrologic studies. Experimental studies (e.g. Rosenberg and Handy 2005) suggest that only a small volume fraction of distributed melt can greatly reduce the bulk strength of a section or rock. The formation of partial melt during high-grade metamorphism, and whether fluid melt continues to form and remain in the rock during periods of decompression and crustal thinning are critical observations needed to test models for melt-enhanced exhumation (e.g., Norlander et al. 2002; Spear 2004; Whitney et al. 2004; Teyssier et al. 2005; Hinchey et al. 2006). This study uses U/Th–Pb

47 geochronology to track and constrain melting and melt crystallization in the context of polyphase
48 exhumation of thickened continental crust.

49 Recent advances in thermodynamic modeling and improvements to our understanding of
50 accessory phase petrogenesis have provided new tools for interpreting accessory phase
51 geochemical, thermobarometric, and geochronologic data (e.g., Kelsey et al. 2008; Spear 2010;
52 Spear and Pyle 2010). Specifically, the ability to model the growth/consumption dynamics of
53 complexly zoned monazite and garnet provides a means to link age and geochemical data to
54 specific segments of a P–T path.

55 The Ruby Mountains–East Humboldt Range (RM–EHR, Fig. 1) metamorphic core
56 complex in northeastern Nevada is located in the central portion of the North American
57 Cordillera hinterland core complex belt (Coney and Harms 1984) and provides an excellent field
58 area to examine anatexis in a greatly exhumed portion of an orogen. Unroofing the Ruby
59 Mountains–East Humboldt Range has exposed some of the deepest portions of the Cordilleran
60 hinterland south of the Idaho batholith (Hodges et al. 1992; McGrew et al. 2000). The
61 structurally deepest portion of the migmatitic infrastructure of the Ruby Mountains–East
62 Humboldt Range is exposed in the northern East Humboldt Range. A complex deformation
63 history obscures the structural assembly of the Winchell Lake fold nappe and of the juxtaposition
64 relationship between the Winchell Lake nappe and the underlying Lizzies Basin block (LBB;
65 Fig. 1). P–T paths based on major and accessory phase thermobarometry, thermodynamic
66 modeling, and porphyroblast zoning analysis indicate somewhat different metamorphic histories
67 for the Winchell Lake nappe and Lizzies Basin block (Hallett and Spear 2014; Fig. 2). In
68 particular, in situ partial melting in the Lizzies Basin block began during a period of heating and
69 crustal thickening, whereas partial melting in the Winchell Lake nappe occurred during a phase

of decompression and slight heating (Hallett and Spear 2014). The absolute timing of partial melting events in the Winchell Lake nappe and the Lizzies Basin block, in the context of the assembly and P–T evolution of these blocks, are needed to establish or refute potential linkages between anatexis, melt residence in the crust, and exhumation.

This contribution presents monazite and zircon geochemistry and SHRIMP U/Th–Pb geochronology for migmatitic gneiss and schist from the northern East Humboldt Range. Specific segments of the P–T paths from Hallett and Spear (2014) for the Lizzies Basin block and Winchell Lake nappe (Fig. 2) are linked with accessory mineral growth using accessory phase + garnet thermometry and in situ monazite and zircon ages for different growth domains. The goal of this study is to improve our understanding of the timescales and nature of exhumation of thickened continental crust that has undergone anatexis. The results demonstrate how integration of these data can provide critical information about the tectonic and thermal history of the Cordilleran hinterland belt and the evolution of metamorphic core complexes.

GEOLOGIC SETTING AND PREVIOUS GEOCHRONOLOGIC STUDIES

The Ruby Mountains–East Humboldt Range high-grade metamorphic and intrusive igneous infrastructure is bound above by a WNW-dipping mylonitic shear zone exposed along the ranges' western flanks. In the northern Ruby Mountains and the East Humboldt Range, allochthonous fold nappes are stacked in a thick succession of penetratively deformed high-grade metamorphic rocks correlated with parts of the Neoproterozoic–Paleozoic miogeoclinal sequence of the eastern Great Basin (McGrew et al. 2000). Fold nappes of the northern Ruby Mountains contain exclusively miogeoclinal sequence rocks and verge generally east or west. The Winchell Lake nappe, in contrast, verges southward and contains in its core Archean–Paleoproterozoic

basement paragneiss and orthogneiss (Lush et al 1988; McGrew and Snoke 2010; Premo et al. 2008, 2010; Henry et al. 2011; McGrew and Premo 2011). All infrastructural metasedimentary rocks are intruded, in greater amounts on lower limbs of fold nappes, by several generations of leucogranites (McGrew et al. 2000; Henry et al. 2011; Howard et al. 2011).

Previous geochronologic studies in the Ruby Mountains–East Humboldt Range are elegantly summarized in Howard et al. (2011; their Table 1). More recent work has focused on the depositional age and detrital signature from paragneisses and quartzites of the Winchell Lake nappe. Late Cretaceous leucogranites of the Ruby Mountains and the possibly contiguous though stratigraphically deeper Lizzies Basin block are interpreted to have formed due to pelite anatexis (Batum 1999; Lee et al. 2003) and crystallized near their source area. However, field observations suggest that crystallization was contemporaneous with deformation, which likely enabled/enhanced melt migration in these rocks (McGrew et al. 2000).

The age of metamorphism in the Ruby Mountains–East Humboldt Range is broadly constrained by intrusive relationships and mineral cooling ages. In the central Ruby Mountains, the intrusion of the Jurassic Dawley Canyon granite (153 ± 1 Ma, U–Pb monazite) has been interpreted to be contemporaneous with localized andalusite metamorphism (Hudec and Wright 1990). In the East Humboldt Range, evidence of pervasive leucogranite magmatism and anatexis is found in both the Winchell Lake nappe and the Lizzies Basin block, leading some workers to interpret in situ partial melting to be a single widespread event that affected the entire crustal section (Lee et al. 2003), perhaps contemporaneous with nappe emplacement (McGrew et al. 2000).

Previous estimates for the timing of peak metamorphism are linked to U–Pb ages interpreted to represent leucosome crystallization. Estimates for the timing of leucosome

crystallization include an isotope dilution–thermal ionization mass spectrometry (ID–TIMS) $^{207}Pb/^{206}Pb$ zircon age of 84.8 ± 2.8 Ma from syn-tectonic leucogranite from the nose of the Winchell Lake nappe (McGrew et al. 2000), and Cretaceous (~91–72 Ma) and Tertiary (~47–32 Ma) U–Pb zircon ages for orthogneiss and paragneiss within the Winchell Lake nappe (Premo et al. 2008, 2010; McGrew and Premo 2011; Metcalf and Drew 2011). Together, these data indicate that zircon growth occurred in Winchell Lake nappe leucogranite dikes and migmatitic Angel Lake orthogneiss near ~80 Ma, and again during a period spanning ~47–32 Ma in paragneiss from the lower limb of the Winchell Lake nappe. In addition, a single ID-TIMS monazite $^{206}Pb/^{238}U$ age of 78 Ma for a biotite schist from the northern Ruby Mountains was reported by Snoke et al. (1979).

An extensive recent study using in situ U–Pb SHRIMP techniques on zircon and monazite from leucogranites collected near Lamoille Canyon in the Ruby Mountains indicates an episodic Late Cretaceous–Paleogene intrusive history that is interpreted to have involved re-melting of earlier generations of leucogranite material (Howard et al. 2011). Different pegmatitic dikes and sills yield zircon and monazite with different crystallization ages clustering near 90 Ma, 69 Ma, 35 Ma, and 30 Ma, interpreted to represent combinations of intrusion of new material and reworking/re-melting of earlier intruded leucogranite. Each of these ages is consistent with intrusive ages for compositionally different magmas of varying abundance throughout the Ruby Mountains–East Humboldt Range (e.g., biotite monzogranite, quartz diorite, quartz gabbro), interpreted to indicate episodic changes in the heat and possibly fluid flux driving local anatexis (Wright and Snoke 1993; Premo et al. 2005; Howard et al. 2011). An additional study of Lamoille Canyon leucogranites documents a decrease in Hf isotope ratios (to strongly negative, ”evolved” εHf values) with zircon U–Pb age that are interpreted to represent

changes in leucogranite source material for Late Cretaceous–Eocene intrusions (Romanoski et al. 2012).

$^{40}Ar/^{39}Ar$ hornblende cooling ages (63–49, 36–29 Ma) provide lower constraints on the age of high-grade metamorphism in the northern East Humboldt Range (McGrew and Snee 1994). Mica and alkali feldspar K–Ar and $^{40}Ar/^{39}Ar$ cooling ages of 27–21 Ma for the northern East Humboldt Range define a regional trend of WNW-younging cooling age pattern across the complex (Kistler et al. 1981; Dallmeyer et al. 1986; Dokka et al. 1986; Wright and Snoke 1993; McGrew and Snee 1994). Stratigraphic constraints and low temperature thermochronology (U/Th–He) in the southern Ruby Mountains indicate a rapid unroofing event associated with mid-Miocene detachment faulting (~17–10 Ma; Colgan et al. 2010).

SUMMARY OF ANALYTICAL METHODS

Samples of metapelitic rock were selected for geochronology based on the presence of garnet and material interpreted as in situ leucosome, as well as the availability of suitable zircon and/or monazite in thin section. The analytical strategy was to examine the compositional variation within monazite and zircon and to determine the U/Th–Pb ages for specific mineral growth events and textural settings (leucosome vs. melanosome, inclusions in garnet). Full monazite compositions were determined for yttrium thermometry using xenotime and major phases, and to compare monazite compositional evolution with theoretical thermodynamic models. Garnet major and trace element zoning analyses were used to track accessory mineral "geochronometer" reactions in the context of the petrogenetic histories presented in Hallett and Spear (2014). Full details of analytical protocol are presented in the supplementary material.

Zircon and monazite grains were drilled from thin sections and imaged (cathodoluminescence [CL] and backscattered electron [BSE] for zircon, BSE and X-ray mapping for monazite) on the Cameca SX100 electron microprobe at Rensselaer Polytechnic Institute. U/Th–Pb ages and trace element compositions of zircon and monazite were analyzed at the Stanford–USGS Micro-Analytical center SHRIMP–RG. Trace element X-ray mapping of garnet in thin section was performed by electron microprobe. Full monazite compositional analyses were done by electron microprobe for samples EH09, EH10, EH31 and EH49. These data were then compared with monazite SHRIMP trace element data in order to correlate age determinations with specific compositional domains fully characterized by electron microprobe analyses. Estimates of OH^- in apatite were calculated from major component electron microprobe analyses (Ca, P, F, Cl) following analytical protocol of Pyle et al. (2002). Trace elements in garnet were analyzed by Laser Ablation–Inductively Coupled Mass Spectrometry (LA–ICMPS) at the Corman Center for Mass Spectrometry at Rensselaer Polytechnic Institute.

SHRIMP U/Th–Pb geochronology results determined for zircon and monazite are generally reported here as ^{207}Pb-corrected ^{206}Pb/^{238}U ages. Zircon standard R33 (~419 Ma) and monazite 44069 (~425 Ma; J. Aleinikoff, personal communication; Aleinikoff et al. 2006) were used. Energy filtering was applied for monazite analyses in order to discriminate against molecular interferences. Zircon and monazite raw ratios were processed using SQUID 2.0 (Ludwig 2009). For coherent age groups interpreted to represent single growth events inverse-variance weighted mean ^{207}Pb-corrected ^{206}Pb/^{238}U ages were calculated using Isoplot for Excel (Ludwig 2003), with errors reported at 95% confidence. Individual spot analysis ages are reported with 2σ errors.

Zircon trace element analyses were performed on the SHRIMP-RG in a session immediately preceding U/Th–Pb analyses, and targeting the same zircon spots. Calibration used Madagascar green zircon (MAD) following the methods of Barth and Wooden (2010). A small set of monazite major and trace elements was analyzed simultaneously with U/Th–Pb analyses. Calibration was performed on monazite standard NAM-2 yielding uncertainties on the order of 0.7–3% (1σ) assuming a homogeneous standard.

SAMPLE DESCRIPTIONS

Winchell Lake nappe samples

The Winchell Lake nappe (WLN; Fig. 1) is a southward closing recumbent fold nappe cored by migmatitic Archean–Paleoproterozoic orthogneiss and paragneiss (Lush et al. 1988; McGrew and Snoke 2010; Premo et al. 2008, 2010; Henry et al. 2011; McGrew and Premo 2011) surrounded by Neoproterozoic–Paleozoic gneisses, schists, marbles, and quartzites (McGrew et al. 2000). In the Winchell Lake nappe, Barrovian metamorphism associated with crustal thickening reached conditions in the garnet + kyanite zone (>680°C, ~9–10 kbar) before the onset of decompression and subsequent anatexis in the sillimanite + alkali feldspar field up to ~740ºC and ~7 kbar (McGrew et al. 2000, Hallett and Spear 2014).

Winchell Lake nappe migmatitic graphite schist (EH09 and EH10). Samples EH09 and EH10 (hereafter referred to as EH09–EH10) are from within 3 meters at an outcrop of tourmaline + graphite-bearing garnet + biotite + sillimanite migmatitic schist from the upper limb of the Winchell Lake nappe. These samples contain relict kyanite and rutile, as well as staurolite and xenotime inclusions in garnet. Few thin plagioclase-rich leucosome segregations are present (Fig. 3a, b). In both leucosome and melanosome plagioclase + biotite + sillimanite

206 reaction coronas commonly surround large (up to 8 mm diameter) garnet porphyroblasts. The
207 samples give similar thermobarometric results and leucosome and melanosome garnet zoning
208 patterns (Hallett and Spear 2014).

209 **Winchell Lake nappe mylonitic paragneiss (EH21).** Sample EH21 is a strongly
210 deformed paragneiss from above Smith Lake near the axis of the Winchell Lake nappe.
211 Leucosomes are not present but quartz ribbons show very biotite-rich, potentially restitic
212 selvedges around them. The peak mineral assemblage is biotite + quartz + sillimanite +
213 plagioclase + garnet + ilmenite + apatite + monazite + zircon [+ melt?]. A small amount of
214 muscovite is also present, in some places oriented oblique to the mylonitic fabric. Muscovite is
215 interpreted as a retrograde phase, grown during crystallization of small amounts of residual melt.
216 Staurolite, and rutile occur as inclusions in garnet. An adjacent calc-silicate layer contains
217 kyanite inclusions in garnet (Hallett and Spear 2014).
218

219 **Lizzies Basin Block samples**

220 Structurally beneath the Winchell Lake nappe, the Lizzies Basin block is apparently
221 contiguous with high-grade metamorphic rocks of the southern East Humboldt Range and
222 northern Ruby Mountains and it contains supracrustal rocks interpreted to be an equivalent
223 section to the miogeoclinal sequence exposed in the northern Ruby Mountains (Howard et al.
224 1979; Snoke 1980; Snoke and Lush 1984; McGrew et al. 2000). Anatexis in Lizzies Basin block
225 metapelites and in the Ruby Mountains occurred at >720°C, ~ 7 kbar with continued heating in
226 the migmatite zone to slightly higher temperatures (~760ºC) than the Winchell Lake nappe (see
227 Hallett and Spear 2014).

Lizzies Basin block garnet paragneiss (EH30 and EH31). These Lizzies Basin block samples are from nearby outcrops (~10 m apart) and contain the same metamorphic assemblage (quartz + plagioclase + biotite + sillimanite + garnet + ilmenite + zircon + monazite [+ melt]). The samples are only slightly migmatitic. Trace muscovite is present, interpreted as a retrograde phase. Most felsic bands contain sparse biotite and little feldspar and are therefore interpreted not as leucosomes but as solid-state formed gneissic bands. Minor leucosomes with very little biotite are present as well, suggesting some in situ melt formed and is preserved.

Lizzies Basin block migmatitic schist (EH45 and EH49). Samples EH45 and EH49 come from ~150 meters apart (along strike) within a coherent garnet + biotite schist unit. Both contain the peak temperature assemblage quartz + plagioclase + biotite + sillimanite + garnet + alkali feldspar + apatite + monazite + zircon + ilmenite [+melt]. Rutile and xenotime are present as small (<100 μm and <40 μm respectively) inclusions in garnet. Xenotime also present in reaction rims around garnet is interpreted as a retrograde mineral. Late muscovite is also present in variable orientations, probably grown during melt crystallization and/or extensional deformation. Only sample EH49 contains leucosomes (Fig. 3c, d) though both samples contain the same mineral assemblage and yield similar thermobarometric results (Hallett and Spear 2014).

Lizzies Basin block sillimanite leucosome (EH48). Sample EH48 is a leucosome within the garnet + biotite schist unit from which samples EH45 and EH49 were collected. EH48 contains quartz + plagioclase + alkali–feldspar + sillimanite + biotite + monazite + zircon + muscovite. Muscovite is a minor phase and is concentrated near fractures, suggesting it may be secondary along with minor hematite. Garnet was not present in this leucosome sample, though adjacent melanosome material does contain garnet.

MONAZITE ZONING AND GEOCHEMISTRY

Monazite BSE imaging and X-ray mapping indicate compositional zoning patterns that result from multiple phases of monazite growth and dissolution, based on core + rim overgrowth patterns and different U/Th–Pb ages for individual domains. Specific compositional domains targeted by electron microprobe and SHRIMP are best categorized based primarily on relative Y, U, and Th content from X-ray mapping. Full electron microprobe analyses for several samples (EH09, EH10, EH31, EH49) allow monazite to be resolved into specific end members (see supplementary material). Chemically and/or texturally distinct monazite domains are numbered in the descriptions that follow.

Winchell Lake nappe samples

Electron microprobe analyses of monazite from both leucosomes and melanosomes of migmatitic graphite schist samples EH09–EH10 show three distinct compositional domains (Fig. 4a). Low-moderate Y cores (monazite 1; $X_{(HREE + Y)PO_4}$ = ~0.051) show some minor variation in Y, Th, and U contents. Two small monazite grains that were analyzed do not preserve monazite (1). Commonly discrete mantles (monazite 2) are lower in $X_{(HREE + Y)PO_4}$ (~0.049). Some of the largest grains show patchy Y, Th, and U zoning with no apparent core–mantle relationship. Most grains have a high Y rim (monazite 3; $X_{(HREE+Y)PO_4}$ = ~0.078), which is generally >20µm thick and discontinuous around the grain. Across the 3 domains, slight core to rim decreases are observed in the coffinite (X_{USiO_4} = ~0.014 to ~0.013) and cheralite ($X_{CaTh(PO_4)_2}$ = ~0.039 to ~0.031) components. The thorite (X_{ThSiO_4}) component is complementary to $X_{(HREE + Y)PO_4}$, with a core–mantle increase (~0.002 to ~0.003) and rim decrease (to ~-0.003).

Monazite from mylonitic paragneiss EH21 occurs mainly in biotite rich domains, with some grains present as inclusions in poikiloblastic garnet. Monazite that appears as inclusions in garnet are low in Y and analyzed REE but moderate in U and Th. Matrix monazite has four distinct compositional domains. Cores (monazite 1) with low to moderate Y, and moderate U and Th (Fig. 4a) are similar in composition to the monazite inclusions in garnet. In a few matrix grains the cores appear to be overgrown/enveloped by slightly lower Y mantles (monazite 2). Two matrix monazite grains that were analyzed by SHRIMP have rims with elevated Y (monazite 3) versus core/mantle material (monazite 1–2). Additionally, thin rims with dramatically higher Y and REE contents are present in matrix grains (monazite 4).

Lizzies Basin Block samples

Monazite from garnet paragneiss samples EH30 and EH31 commonly contain 3 compositional domains. Several analyzed monazite grains contain a moderately low Y core (monazite 1), which has a distinctly low coffinite component (0.006–0.012; EH31). Monazite (2) overgrows monazite (1) or forms the cores of some EH30 and EH31 grains, showing a moderate variation in Y content with either irregular zoning or rarely pseudo-oscillatory zoning of Y enrichment (Fig. 5a). EH31 monazite (2) shows a rim-ward decrease in the coffinite (~0.022 to ~0.015) and cheralite (~0.056 to 0.043) components, with little change in thorite (~-0.010). Complementary increases in EH31 monazite (2) $X_{(HREE+Y)PO_4}$ are observed (~0.051 to ~0.056). High Y rims (EH31 $X_{(HREE+Y)PO_4}$ up to ~0.082; monazite 3), though not as high Y as in other East Humboldt Range samples, form irregular overgrowths in some grains. Some monazite (3) overgrowths crosscut internal zoning patterns and/or fill in recessed surfaces of grain cores.

296 Monazite (3) rims are more prominent in fine-grained high strain zones, and they are thickest at
297 grain tips.

298 Monazite from migmatitic schist samples EH45 and EH49 contains 4–5 compositional
299 domains (see Fig. 5a). Monazite (1), as in samples EH30–EH31, is comprised of irregularly
300 shaped, low U (< 5000 ppm), patchy Th zoned cores. EH49 monazite (1) is low in coffinite
301 (0.010–0.018) and moderate in cheralite (0.033–0.046) and $X_{(HREE+Y)PO_4}$ (0.041–0.064).
302 Monazite zones (2–4) are characterized by increasing Y content between each compositional
303 domain. In EH49 monazite, decreases in coffinite (from ~0.023 to ~0.017) and cheralite (~0.052
304 to ~0.039), with complementary increases in thorite (-0.017 to -0.009) and $X_{(HREE+Y)PO_4}$ (~0.031
305 to ~0.077) are observed. Monazite zones (2) and (3) form mantles, with low Y (< 0.5 wt%)
306 monazite (2), and moderate Y (> 0.5 wt%) monazite (3). Analyses of the highest Y rim domains
307 (4–5) observed on EH49 X-ray maps give $X_{(HREE+Y)PO_4}$ values that are generally lower (0.065–
308 0.085) than those for high Y rims found on monazite from other samples (EH09–EH10 and
309 EH31). Monazite (5) is only distinguished from monazite (4) on the basis of age, discussed
310 further below.

311 Sillimanite leucosome sample EH48 monazite shows patchy zoning in BSE images, and
312 moderate to high Y cores. Chemical zoning observations from EH48 are based on X-ray
313 mapping and SHRIMP trace element data. Grains with slightly elevated Y rims are observed,
314 though nearly all analyses were high in Y (>1.5 wt%) compared with core and mantle monazite
315 from other samples (~0.5–1.0 wt%). One large monazite grain shows thin, irregular, very high U
316 zones not observed in other grains. Slight patchy variation in Th content is observed (Fig. 5a).
317 Locally high U, Th and Y core material is present in some grains, though zones are too small for
318 SHRIMP analysis.

ZIRCON AND MONAZITE U/TH–PB RESULTS

Monazite geochronology results are presented below for each sample. Zircon geochronology results from Winchell Lake nappe samples EH09 and EH10 as well as for Lizzies Basin block sample EH49 are also discussed. SHRIMP Geochronology results for zircon and monazite are included as supplementary material. The results of U/Th–Pb monazite and zircon geochronology of compositionally and/or texturally distinct populations are given in Figures 4–7 and summarized in Figure 8.

Winchell Lake nappe samples

EH09–EH10. Zircon grains from migmatitic graphite schist samples EH09–EH10 are generally small (<70 μm in length) and display faint oscillatory-like CL domains, in most grains surrounding an easily distinguished low CL core (Fig. 6a). All analyses yield very low Th concentrations (≤ 30 ppm). Concordant ^{207}Pb-corrected ^{206}Pb/^{238}U age results from oscillatory-zoned zircon spread from 59.2 ± 7.0 to 77.2 ± 1.6 Ma for EH09 (n = 7) and 58.9 ± 3.6 to 77.4 ± 12.4 Ma for EH10 (n = 10; Fig. 6b). Only 1 of 6 leucosome zircon analyses from EH10 yielded a ^{207}Pb-corrected ^{206}Pb/^{238}U age younger than 72 Ma whereas 8 of 11 melanosome zircon analyses yield ages ≤ 72 Ma.

Analyses of EH09–EH10 monazite (1) are generally concordant in U–Pb space with minor mixing toward common Pb (Fig. 4b). Monazite (1) ^{207}Pb-corrected ^{206}Pb/^{238}U ages spread from 86.8 ± 5.6 to 75.9 ± 1.6 Ma for EH10 (n = 14), and a single analysis from EH09 yields an age of 80.3 ± 6.0 Ma. A weighted mean ^{207}Pb-corrected ^{206}Pb/^{238}U age using all monazite (1) analyses from EH10 is 79.8 ± 2.2 Ma (n = 14, MSWD = 4.0). Excluding the youngest monazite

(1) analysis, which gives considerable uncertainty in $^{207}Pb/^{206}Pb$ and could represent a mixed domain, gives a weighted mean ^{207}Pb-corrected $^{206}Pb/^{238}U$ age of 82.8 ± 1.3 Ma (n = 13, MSWD = 0.65). Monazite (2) domains were volumetrically minor and therefore difficult to analyze. Four monazite (2) analyses yield ages that are consistently younger than monazite (1), two of which are discordant due to moderate common Pb contents. ^{207}Pb-corrected $^{206}Pb/^{238}U$ ages for this compositional domain spread from 59.9 ± 4.4 to 71.8 ± 4.0 Ma. Rim (monazite 3) analyses yield the youngest ages and the most discordant results in a Tera–Wasserburg plot (Fig. 4b). ^{207}Pb-corrected $^{206}Pb/^{238}U$ ages range from 32.3 ± 5.8 to 41.7 ± 10.4 (n = 4). Re-examination of spot locations indicated that most monazite (3) analyses overlapped grain boundaries and partly sampled non-monazite phases.

Zircon cores are interpreted as pre-metamorphic and probably detrital, based on CL contrast. Monazite (1) growth largely predates zircon ages from these samples. Apparent clustering of leucosome zircon ages near 72–73 Ma with melanosome zircon ages spreading to ~60 Ma may indicate that leucosome crystallization occurred by 72 Ma whereas zircon growth in melanosomes may have continued until close to ~60 Ma. In contrast, no distinguishable age or compositional difference was recognized between monazite of different textural settings (leucosome vs. melanosome, e.g., Fig. 3b). Monazite (1) growth is interpreted to have occurred during a single event at 82.8 ± 1.3 Ma. Monazite (2) growth appears to be coeval with zircon crystallization in leucosomes and melanosomes. Monazite (3) growth post-dates all zircon ages determined for EH09–EH10 though analyses appear to have incorporated high common Pb and/or decreased Th by intersecting grain boundaries and/or adjacent phases.

EH21. Zircon from mylonitic paragneiss EH21 was not analyzed due to a lack of suitable material. Four SHRIMP analyses were performed on two monazite inclusions in poikiloblastic

garnet. The three oldest analyses give ^{207}Pb-corrected ^{206}Pb/^{238}U ages of 72.4 ± 3.0, 71.4 ± 4.8 and 70.7 ± 4.4 Ma (Fig. 4c). The youngest monazite inclusion analysis gives a ^{207}Pb-corrected ^{206}Pb/^{238}U age of 65.3 ± 14.0 Ma, with a large uncertainty and a low U content. This spot was located on a portion of an inclusion grain that makes contact with the quartz-rich matrix.

All high U and Th matrix monazite analyses (monazite 1 + 3) give ages that spread along U–Pb concordia with several slightly discordant analyses. ^{207}Pb-corrected ^{206}Pb/^{238}U ages range from 64.7 ± 1.0 to 70.7 ± 2.6 Ma. Two ages for monazite (3) fall near the younger end of this range: 64.7 ± 3.0 and 69.9 ± 4.2 Ma. A weighted mean ^{207}Pb-corrected ^{206}Pb/^{238}U age for 6 analyses of monazite (1) and (3) is 65.6 ± 2.0 Ma (MSWD = 3.1; Fig. 4c). Monazite (4) generally gives Eocene ages with some analyses that are high in common Pb. The two lowest common Pb (<1% ^{206}Pb) analyses give ^{207}Pb-corrected ^{206}Pb/^{238}U ages of 34.8 ± 0.6 and 38.4 ± 0.7 Ma.

The analyzed monazite inclusions in EH21 garnet occur in a poikiloblastic crystal that may have grown entirely during anatexis. The three-dimensional geometry of inclusions and matrix embayments in this grain presents difficulty in interpretation of potential monazite chemical communication with matrix phases and possible recrystallization. It is likely that the youngest grain, in contact with matrix quartz, recrystallized with matrix monazite and may not reflect the inclusion age. In addition, the older inclusion ages (Fig. 4c) overlap within uncertainty of matrix ages, perhaps explained by open chemical communication and growth with matrix monazite. Another possibility is that inclusion monazite grew on the prograde path but a rapid cycle for decompression, melting, and melt crystallization cannot be deciphered with respect to matrix monazite without better analytical precision. The discordance of matrix monazite (1+3) is interpreted to reflect the likely presence of some common Pb.

388

389 **Lizzies Basin Block samples**

390 **EH30 and EH31.** The garnet paragneiss samples did not yield sufficient zircon for
391 conclusive analyses. All EH30 and EH31 U/Th–Pb monazite analyses give consistent ^{207}Pb-
392 corrected ^{206}Pb/^{238}U and ^{204}Pb-corrected ^{208}Pb/^{232}Th ages. Two EH31 monazite core analyses
393 (monazite 1) give ^{207}Pb-corrected ^{206}Pb/^{238}U ages of 147.5 ± 9.8 and 157.6 ± 3.6 Ma (Fig. 5a);
394 the former is from an inclusion in garnet and contains a low Y overgrowth. A monazite (1)
395 analysis from EH30 gives a ^{207}Pb-corrected ^{206}Pb/^{238}U age of 139.3 ± 5.0 Ma. Two EH30
396 monazite analyses overlap core and mantle material, giving discordant ages and were discarded.
397 Monazite (2) analyses give ^{207}Pb-corrected ^{206}Pb/^{238}U ages of 91.7 ± 6.2 Ma and 92.7 ± 4.8 for
398 EH30 and a spread in ^{206}Pb/^{238}U ages from 76.5 ± 4.0 Ma to 89.4 ± 9.2 for EH31 (n = 4). The
399 oldest monazite (2) analysis from sample EH31 (89.4 ± 9.2 Ma ^{206}Pb/^{238}U age) is from an
400 inclusion in EH31 garnet. Three high Y rim (monazite 3) analyses give ^{207}Pb-corrected
401 ^{206}Pb/^{238}U ages of 28.7 ± 2.8 (EH31), 34.6 ± 5.8 (EH31), and 35.9 ± 2.4 Ma (EH30).
402 Monazite ages from EH30 and EH31 are interpreted to represent at least 3 phases of
403 growth, with initial (monazite 1) growth during a relict Jurassic metamorphic event. It is difficult
404 to determine whether monazite (2) ages should be interpreted as a single, possibly protracted
405 growth event or unresolved phases of growth. In light of matrix monazite (2) giving similar ages
406 to those of inclusions of monazite (2) in garnet, a broad range in monazite (2) ages, and a better
407 record of monazite growth phases in EH45 and EH49 (discussed in detail below), it seems likely
408 that ages for monazite (2) span two unresolved growth episodes.
409 **EH45 and EH49.** Unfortunately, a lack of suitable material only allowed for 7 SHRIMP
410 zircon analyses from migmatitic schist sample EH49, and none from migmatitic schist sample

411 EH45. EH49 zircon grains were generally small (mostly < 50 μm). Ages calculated are therefore
412 not statistically robust, and independent zircon growth domains are difficult to distinguish.
413 The 3 analyses of zircons extracted from material interpreted to be in situ leucosome,
414 show fairly uniform CL apart from one dark core domain that was not analyzed. These
415 leucosome zircons give ^{207}Pb-corrected ^{206}Pb/^{238}U ages of 61.4 ± 5.6, 61.7 ± 7.8, and 64.7 ± 3.7
416 Ma. Three of four melanosome zircon grains show brighter core domains. One high common Pb
417 core was analyzed, giving a ^{204}Pb-corrected ^{207}Pb/^{206}Pb age of 1364 ± 80 Ma. Outboard of bright
418 core domains, melanosome zircon shows a dark CL domain surrounded by a less dark rim
419 domain (Fig. 7a). This zircon has a more euhedral and elongate shape common to igneous zircon
420 (Corfu et al. 2003) than the subhedral to equant shape of leucosome zircon. Three SHRIMP
421 analyses of the rim domain give ^{207}Pb-corrected ^{206}Pb/^{238}U ages of 81.1 ± 6.6, 81.3 ± 5.5 and
422 86.7 ± 13.4 Ma.
423 Leucosome EH49 zircon grains are small but morphology may indicate these grains grew
424 via metamorphic as opposed to igneous processes. Specifically, the 3 leucosome grains are more
425 rounded than melanosome zircon, slightly irregularly shaped, and contain regions that appear to
426 show sector zoning (Fig. 6a) and regions of pseudo-concentric zoning patterns that follow grain
427 boundaries. The brighter core domains in EH49 melanosome zircon are interpreted as relict
428 detrital zircon. Based on grain morphology, it appears plausible that melanosome rim zircon
429 grew during a melt crystallization event.
430 As discussed above, five compositional domains are recognized and distinguishable in
431 samples EH45 and EH49 (Fig. 5a). However, monazite (2) and (3) discussed above cannot be
432 clearly distinguished in terms of age and hence age data from these compositional domains are
433 combined in the ages presented here. ^{207}Pb-corrected ^{206}Pb/^{238}U and ^{204}Pb-corrected ^{208}Pb/^{232}Th

ages are generally consistent for all SHRIMP analyses. Because of its irregular zoning pattern (Fig. 5a), only 3 analyses were possible in monazite (1) cores, including one monazite inclusion in garnet. Monazite (1) gives ^{207}Pb-corrected ^{206}Pb/^{238}U ages that are nearly consistent: 123.6 ± 12.4 Ma (EH49), 125.1 ± 5.0 Ma (EH45), and 139.6 ± 7.4 (EH49) Ma. Three analyses of monazite (2–3) from EH45 give ^{207}Pb-corrected ^{206}Pb/^{238}U ages that range from 82.9 ± 7.1 to 96.5 ± 8.0 Ma. Seven analyses of monazite (2–3) from EH49 give ^{207}Pb-corrected ^{206}Pb/^{238}U ages that range from 81.0 ± 3.8 to 94.0 ± 5.8 Ma. This includes two monazite grains extracted from thin leucosomes within EH49 which show similar zoning patterns to all melanosome zircons and give monazite (2–3) ages on the younger end of the range, 82.7 ± 3.2 and 81.0 ± 3.8 Ma. High Y rims (monazite 4) are thin and were therefore difficult to analyze. Four rim analyses were concordant in U–Pb space and give a spread in ^{207}Pb-corrected ^{206}Pb/^{238}U ages from 68.2 ± 4.7 to 74.4 ± 6.8 Ma for EH45 and an age of 65.0 ± 3.6 Ma for EH49. Two additional (EH45) analyses of high Y rims give high common Pb (strongly discordant) analyses (combined as monazite 5?; Fig. 5a, c). Correcting these for common Pb using ^{207}Pb gives ^{206}Pb/^{238}U ages of 41.6 ± 7.4 and 37.3 ± 4.7 Ma.

The limited number of monazite (1) ages is interpreted to represent pre-Late Cretaceous monazite growth, possibly correlated to Jurassic to Early Cretaceous (?) monazite ages from EH30 and EH31. Compositionally distinct monazite zones (2) and (3) give ages that overlap within uncertainty. However, based on compositional distinctions discussed above, the results from each domain can be grouped separately, interpreted to reflect monazite growth events with a significant ages, despite overlap in age uncertainty. U–Th–Pb analyses sampling exclusively monazite (2) from EH45 and EH49 give ages from 96.5 ± 8.0 to 86.4 ± 6.6 Ma. Exclusive monazite (3) analyses from EH45 and EH49 give ages from 85.0 ± 4.4 to 81.0 ± 3.8 Ma.

Monazite (4–5) is interpreted to represent growth during retrograde metamorphism with possible reheating.

EH48. EH48 monazite rims were too thin for analysis. Eight monazite core analyses spread along U–Pb concordia. ^{207}Pb-corrected ^{206}Pb/^{238}U ages spread from 73.3 ± 4.2 to 84.7 ± 6.8 Ma (Fig. 5d). Excluding the youngest analysis, which shows discordance between ^{206}Pb/^{238}U and ^{208}Pb/^{232}Th ages and may represent Pb loss, gives a weighted mean age of 80.1 ± 1.4 Ma (n = 7, MSWD = 1.06). No significant age difference is recognized across variable Th domains (Fig 5a).

TRACE ELEMENT GEOCHEMISTRY

Zircon Rare Earth Elements

Refractory portions of detrital zircon grains are commonly preserved in metamorphic rocks as relict cores overgrown by new zircon (Williams 2001; Dempster et al. 2008). Overgrowths can either precipitate from an anatectic silicate melt ("igneous zircon" sensu stricto), grow exclusively due to solid-state processes, or precipitate from metamorphic fluid ("metamorphic zircon"; Hoskin and Black 2000; Hoskin and Schaltegger 2003; Whitehouse and Kamber 2003). Zircon major and trace element compositions can help distinguish between these growth processes, and may help identify zircon grown in equilibrium with garnet (Rubatto 2002; Hoskin and Schaltegger 2003; Whitehouse and Platt 2003). We present zircon trace element data here as a means to compare compositional information for zircon with different crystallization ages and across different textural settings.

Non-detrital zircon from Winchell Lake nappe samples EH09 and EH10 shows rare earth element (REE) compositions that vary between two end member patterns (Fig. 9a, b). Pattern (1)

is characterized by a generally continuous increase in chondrite normalized REE abundance with atomic number (positive slope). Pattern (2) represents a zero slope for heavy REE, approaching uniform chondrite-normalized concentrations for Dy–Yb. In EH09 and EH10, pattern (1) is observed for both leucosome and melanosome zircon, and in zircon giving a wide range of ^{207}Pb-corrected ^{206}Pb/^{238}U ages. Zircon patterns "shallow out" or approach pattern (2) in 5 of 11 EH10 analyses with no apparent relationship to textural setting or age. EH09 zircon shows continuous increases with atomic number, but slopes vary toward fairly shallow (skew toward pattern 2).

Most EH49 zircon analyses show positive HREE slopes that are similar to those from sample EH09, spread between pattern (1) and (2) end members. However, 2 of 7 analyses show a different pattern (pattern 3) characterized by an inflection in REE abundance at Dy, with Dy being the most abundant REE and heavier REE decreasing in abundance with higher atomic number. These zircon grains were extracted from leucosome domains and give the youngest ages from this sample. The other leucosome zircon analysis gives a REE distribution closer to pattern (1).

Garnet Rare Earth Elements

Garnet is present in leucosome and melanosome portions of analyzed migmatitic samples EH09–EH10 and EH49. Zoning patterns and grain morphology are similar for both textural settings. Garnet HREE zoning is correlated with mapped Y zoning (Fig. 9d; see also Hallett and Spear 2014). Cores from Winchell Lake nappe melanosome garnet (samples EH09–EH10; Fig. 9e, f) are enriched in HREE, whereas the higher X_{Grs} mantles are strongly depleted in HREE. An increase in HREE along preserved portions of the garnet rim is also observed. The same patterns are observed for leucosome garnet from EH09 (see Supplementary Material). Less variation is

503 observed and core enrichment is much less pronounced in EH49 (Fig. 9g) versus EH09 and
504 EH10, with over an order of magnitude difference between the two sample locations.
505
506 **Zircon/Garnet Trace Element Interpretation**
507 The garnet trace element analyses are interpreted to indicate the loss of xenotime from
508 the stable assemblage following garnet core growth but prior to mantle growth. Xenotime had
509 acted to buffer initially high HREE+Y garnet growth, which shifted the reactive bulk
510 composition to strongly HREE-depleted by sequestering HREE and Y in the garnet core. High
511 X_{Grs}, low HREE garnet mantles are consistent with garnet growth at temperatures above those
512 for staurolite stability, based on thermodynamic modeling and Zr–in–rutile thermometry of rutile
513 inclusions in specific garnet compositional domains and kyanite (Hallett and Spear 2014).
514 Moderate HREE rims in Winchell Lake nappe garnet are interpreted to have grown during
515 anatexis after some garnet resorption had taken place during decompression that led to melting
516 (Hallett and Spear 2014). The mantle–rim increase in HREE may represent the breakdown of
517 REE-bearing apatite and/or zircon during melting. Higher HREE rims are thin or absent from
518 analyzed Lizzies Basin block garnet because of retrograde garnet resorption evidenced by strong
519 Mn diffusion profiles (Hallett and Spear 2014).
520 The garnet present in these rocks grew on the prograde path (Hallett and Spear 2014),
521 while zircon, presumably detrital (Rubatto et al. 2001), was likely a passive observer. Garnet
522 growth above the solidus occurred due to continuous biotite dehydration melting while the rocks
523 of the East Humboldt Range were still undergoing heating. Increasing zircon solubility in the
524 melt phase with heating (e.g. Kelsey et al. 2008) suggests that zircon would dissolve during
525 melting that produced garnet, and therefore detrital zircon may have acted as a minor source for

526 elevated HREE garnet rims. At the start of cooling and melt crystallization, garnet consumption
527 and simultaneous zircon growth would occur. This could theoretically set up a process whereby
528 the silicate melt facilitates chemical communication between dissolving garnet and growing
529 zircon. A partitioning relationship for REE in zircon and garnet in equilibrium is documented in
530 high-grade migmatitic rocks (Rubatto 2002; Whitehouse and Platt 2003; Harley and Kelly 2007).
531 However, it is a stretch to consider that the silicate melt, for which there is evidence that it was
532 partially removed from the system, enabled an equilibrium relationship between resorbing garnet
533 and growing zircon. Furthermore, garnet resorption is demonstrated to be irregular in terms of
534 consuming portions of garnet grains of different composition (Hallett and Spear 2014). Therefore
535 no particular garnet composition could be defined for an apparent equilibrium relationship
536 without relying on assumptions and oversimplifications.
537 EH09 and EH10 zircon patterns do not indicate a coherent shift in zircon REE
538 compositions with age, consistent with zircon growth due to a single growth process such as
539 precipitation from a silicate melt upon cooling. We suggest it is possible that variation in zircon
540 REE compositions reflect localized kinetic processes of garnet resorption and melt
541 formation/extraction from the system. Pattern (3) leucosome zircon from Lizzies Basin block
542 sample EH49 (Fig. 9c) is reminiscent of subsolidus zircon grown/recrystallized in the presence
543 of garnet (Schaltegger et al. 1999; Hoskin and Schaltegger 2003; Whitehouse and Platt 2003).
544 Whereas these grains occur within leucosome domains, it is possible that they represent
545 subsolidus zircon recrystallization. With only a small number of grains of this age, their
546 significance is inconclusive.
547

548 **TITANIUM-IN-ZIRCON THERMOMETRY**

549 The Ti-in-zircon thermometer (Watson et al. 2006; Ferry and Watson 2007) was applied
550 to East Humboldt Range zircons. The Ti content of zircon ranges from 1.5 ± 0.1 ppm to ~13.2 ±
551 0.5 ppm in the Winchell Lake nappe samples and 1.5 ± 0.1 ppm to ~14.2 ± 0.5 ppm in the
552 Lizzies Basin block samples. Calculations of Ti–in–zircon temperatures were performed using
553 the calibration of Ferry and Watson (2007) and a range of Ti activities (see Fig. 10 and
554 supplementary data).
555 Calculated temperatures (Fig. 10) are generally consistent with those (610 ± 88ºC)
556 derived from zircon grown in a global representation of peraluminous granitic rocks, which
557 include temperatures that fall below H_2O-saturated melting equilibria (Fu et al. 2008). No clear
558 correlation between Ti concentration (or temperature) and U–Pb age is observed (Fig. 10). A
559 single zircon analysis from each leucosome and melanosome from EH09–EH10 and 2 of 3
560 melanosome zircon grains from EH49 give higher temperatures (>750ºC). The range of zircon
561 temperatures in these rocks partly overlaps with the monazite + Y–Al garnet (YAG)
562 thermometry results from monazite interpreted to represent melt crystallization, discussed below.
563 Uncertainty with respect to (1) the extent of equilibrium behavior of Ti in these samples and (2)
564 the effective a_{Ti} for rocks containing stable ilmenite and (likely) some metastable rutile (Hallett
565 and Spear 2014), prevents a more rigorous application of Ti thermometry.
566

567 **YTTRIUM THERMOMETRY AND MONAZITE PARAGENESIS**

568 Yttrium thermometry involving the phases garnet, xenotime, and monazite can be used to
569 help constrain the P–T conditions of monazite growth and thus the significance of the monazite
570 ages (e.g. Gratz and Heinrich 1997; Pyle and Spear 1999, 2000; Pyle et al. 2001; Foster et al.
571 2004). Xenotime and garnet are assumed to coexist as evidenced by inclusions of xenotime in the

572 cores of garnet with high YAG component (e.g. samples EH09, EH10, EH49). According to the
573 models of Spear and Pyle (2010; see also Fig. 11) monazite in these types of low-Ca rocks may
574 form at low grades so it may also be assumed that monazite and xenotime coexist at grades
575 below garnet stability. Xenotime typically reacts out during garnet growth and typically appears
576 again during/following garnet resorption (Spear and Pyle, 2010; Fig. 11). This is evidenced by
577 steep declines in the YAG component of garnet outward from the core and the absence of
578 xenotime inclusions in the mantles of these garnets or in the matrix. Again following Spear and
579 Pyle (2010), in conditions under which monazite and garnet are stable and xenotime is not,
580 monazite and garnet do not grow contemporaneously (Fig. 11a, c). In the absence of allanite,
581 further monazite growth is typically restricted to conditions of melt crystallization, garnet
582 resorption, or both (Spear and Pyle 2010; Spear 2010). Sharp compositional boundaries observed
583 in X-ray maps (see Figs. 4a, 5a) suggests that diffusion of Y (plus U, Th and likely HREE) in
584 monazite is slow enough to preserve growth compositions. These guidelines are used in
585 assessing the validity of YAG–xenotime, xenotime–monazite, and monazite–garnet thermometry
586 (Table 1). In addition, theoretical models of equilibrium assemblages and phase compositions for
587 a pelite of similar bulk composition to Winchell Lake nappe sample EH10 (Fig. 11; as modeled
588 by Spear and Pyle 2010) were calculated using a low Y composition assuming the majority of
589 bulk Y became isolated in garnet cores. These models are therefore best suited to the higher
590 temperature garnet-bearing assemblages.
591

592 **Monazite paragenesis in the Winchell Lake nappe**

593 Garnet cores from samples EH09–EH10 grew prior to a pre-anatectic phase of kyanite +
594 staurolite metamorphism (Hallett and Spear 2014), are high in Y (up to 4400 ppm) and HREE

595 (see Fig. 9d, e), and contain xenotime inclusions. Additionally, very small monazite inclusions
596 are present in this high Y garnet domain. Matrix monazite cores in these rocks (monazite 1, Fig.
597 4a) contain X_{YPO_4} of 0.027 ± 0.003 and a X_{HREEPO_4} of 0.024 ± 0.002 (1σ) and monazite of similar
598 composition is also found as inclusions in garnet. Monazite core + xenotime temperatures for
599 these rocks (363 ± 38ºC for EH09, 437 ± 14ºC for EH10) are below the garnet core temperature
600 (470 ± 7ºC for EH09, 498 ± 3ºC for EH10) inferred from YAG-xenotime thermometry,
601 consistent with the above assumptions about monazite and xenotime paragenesis (e.g. segment 1,
602 Fig. 11c).

603 EH09–EH10 garnet growth occurred by xenotime + chlorite (± chloritoid) consuming
604 reactions until xenotime was exhausted, after which monazite is predicted to have been partially
605 consumed (Fig. 11c; Spear and Pyle 2010). Garnet mantles grew during a phase of higher
606 pressure metamorphism during and/or following the breakdown of staurolite, and in the presence
607 of kyanite (Hallett and Spear 2014). This prograde segment of the P–T path shallowly crossed
608 isopleths of monazite abundance (see Fig. 11c), and thus should have resulted in minor
609 resorption of monazite grains (Spear and Pyle 2010). Therefore, similar to zircon paragenesis
610 (see above), no monazite is interpreted to have grown during this P–T segment.

611 The theoretical modeling predicts that resumed monazite growth would occur during
612 retrograde cooling above the solidus (segment 2, Fig. 11c) by one of the following reactions:

613 $$\text{Grt} + \text{Kfs} + \text{melt} = \text{Bt} + \text{Pl} + \text{Sil} + \text{Qtz} + \text{Mnz} \pm \text{Ap} \quad (1)$$

614 or

615 $$\text{Sil} + \text{Kfs} + \text{melt} = \text{Ms} + \text{Pl} + \text{Qtz} + \text{Mnz} \pm \text{Ap}. \quad (2)$$

616 Very little muscovite is present in these rocks, suggesting that reaction (1) dominated the in situ
617 melt crystallization process, due to significant loss of melt prior to reaching conditions for

618 reaction (2). Application of the monazite + garnet thermometer of Pyle et al. (2001) requires
619 compositional information about all phases involved in the reaction:

620 $$\text{YAG (Y + Al Grt)} + \text{(OH)-Ap} + \text{Qtz} = \text{Grs} + \text{An} + \text{YPO}_4\ \text{Mnz} + \text{H}_2\text{O}. \quad (3)$$

621 Apatite is relatively abundant (~0.3–0.4 % by volume) and occurs as inclusions in garnet as well
622 as in the both the leucosome and melanosome matrix. Matrix apatite is rich in fluorine, giving a
623 relatively low X_{OH} (<0.10). Plagioclase rims enriched in X_{An} and matrix apatite are interpreted to
624 have grown with monazite during melt crystallization. It is also evident that no portion of the
625 zoned garnet grew in direct equilibrium with monazite formed during melt crystallization.
626 Therefore, the garnet rim composition was be used as an approximation of the effective garnet
627 composition during monazite growth. Notwithstanding these assumptions, the application of the
628 YAG-monazite thermometer to the anatectic, low $X_{(Y+HREE)PO_4}$ monazite (monazite 2, from
629 EH09–EH10) yields 678 ± 19ºC for EH09 and 694 ± 21ºC for EH10 (Table 1). These
630 temperatures are consistent with phase equilibria calculations of the solidus temperature (e.g.
631 Fig. 11; Hallett and Spear 2014) and support the inference that monazite (2) ages reflect the time
632 of melt crystallization.

633 High Y zones are observed on the rims of a number of grains (e.g. monazite 3, Fig. 4a).
634 Similar high-Y rims on monazite grains in migmatitic rocks have been suggested to represent
635 melt crystallization (Pyle and Spear 2003; Pyle et al. 2005; Kelly et al. 2006) resulting from the
636 release of Y during garnet breakdown (e.g. Kohn et al. 2005). However, based on the apparent
637 lack of zircon rims of similar age in these rocks our preferred interpretation is that these high
638 $X_{(Y+HREE)PO_4}$ rims represent breakdown of garnet during subsolidus retrograde metamorphism by
639 a reaction such as:

640 $$\text{Y-bearing Grt} + \text{Kfs} + \text{(OH)-Ap} \pm \text{H}_2\text{O} = \text{Bt} + \text{Pl} + \text{Sil} + \text{Qtz} + \text{Mnz} \quad (4)$$

641 or

642 $$\text{Y-bearing Grt} + \text{Ms} + \text{Ap} = \text{Sil} + \text{Bt} + \text{Pl} + \text{Mnz} \quad (5).$$

643 The high Y rims on monazites that give Eocene–Oligocene ages may therefore be subsolidus
644 retrograde monazite, grown during a phase of decompression at pressures that are above
645 xenotime stability. Furthermore, xenotime is observed in embayments and reaction coronas
646 around garnet (e.g. sample EH10; see Fig. 12) suggesting that breakdown of garnet during
647 retrograde hydration released sufficient Y to stabilize xenotime.

648 Calculated monazite + xenotime temperatures based on the high-Y monazite rims yield
649 525 ± 47ºC for EH09 and 558 ± 28ºC for EH10 (Table 1) and are consistent with this subsolidus
650 retrograde monazite model. The Eocene–Oligocene ages of these high-Y rims therefore are
651 believed to reflect this retrograde event. Significantly, these ages fall between the emplacement
652 ages for quartz diorite (~40 Ma) and the biotite monzogranite (~29 Ma; Fig. 1; Wright and Snoke
653 1993) in the region. Therefore, this intrusive magmatism (Armstrong and Ward 1991; Wright
654 and Snoke 1993) may have introduced heat and fluids that drove the retrograde event.

655

656 **Monazite paragenesis in the Lizzies Basin block**

657 Samples EH45 and EH49 contain garnet with cores that host monazite and xenotime and
658 show relatively high Y+HREE (Fig. 9f; Hallett and Spear 2014), though X_{YAG} is far lower than
659 for the xenotime-bearing garnet cores from the Winchell Lake nappe (~250 vs. 1500–4000 ppm).
660 A calculated YAG + xenotime temperature of 564 ± 7ºC for sample EH49 is higher than for
661 Winchell Lake nappe garnet core growth (Table 1) and broadly consistent with the garnet isograd
662 on the pseudosection for these rocks (Hallett and Spear 2014). The absence of relict prograde
663 phases or inclusion suites prevents the early portion of the P–T path from being defined.

664 Monazite (2) from sample EH49 (Fig. 5a,c) may have grown in equilibrium with
665 xenotime, based on the presence of monazite and xenotime inclusions in EH49 garnet cores. In
666 one location, a monazite inclusion (grain 49b13) that contains a monazite (1) core (136.2 ± 4.8
667 Ma) and a very thin, more moderate Y rim that is probably monazite (2), is in direct contact with
668 xenotime. A calculated monazite + xenotime temperature of 445 ± 28ºC is consistent with
669 monazite (2) growth below the garnet isograd on the prograde path. Another low Y monazite (2)
670 inclusion from sample EH31 garnet also gives an age (89.4 ± 9.2 Ma) that is consistent with that
671 of monazite (2+3) from EH45 and EH49, suggesting that the broad age range for monazite (2)
672 growth in EH30–EH31 in part pre-dates garnet growth.
673 Linking monazite compositions with preserved garnet zones is difficult in EH49, and it is
674 evident from petrography and compositional zoning maps (Hallett and Spear 2014) that
675 significant garnet resorption has removed portions of garnet porphyroblasts that may have grown
676 in equilibrium with, or during breakdown of monazite (2). However, no obvious monazite
677 resorption texture (see Fig. 5a) is observed between monazite (2) and (3). Therefore, it is
678 plausible that the prograde P–T path for the Lizzies Basin block followed a slope near that of
679 monazite abundance isopleths, as shown in theoretical models (Fig. 11c), resulting in little net
680 growth and/or consumption of monazite in some Lizzies Basin block pelites prior to anatexis.
681 As in the Winchell Lake nappe samples, garnet rim compositions were taken as an
682 approximation of the equilibrium garnet composition during monazite growth above xenotime
683 stability. Monazite (3) (Fig. 5a,c), presumed to have grown above xenotime stability, was used
684 with average garnet rim, apatite, and plagioclase compositions to apply the YAG + monazite
685 thermometer of Pyle et al. (2001) yielding a temperature of 672 ± 25ºC (Table 1). Interpretation
686 of the significance of monazite (3) and this thermometry result is difficult. One possibility is that

687 monazite (3) represents prograde monazite growth due to the breakdown of another accessory
688 mineral such as allanite (Corrie and Kohn 2008). However, the estimated bulk composition of
689 EH49 (see Hallett and Spear 2014) is apparently too Al-rich and Ca-poor to stabilize allanite
690 (Spear 2010), and no relict allanite is observed in these rocks.
691 Alternatively, the growth of monazite (3) may have occurred during melt crystallization.
692 In this scenario, monazite resorption would have accompanied partial melting to peak
693 temperature, followed by slightly higher Y monazite overgrowths (monazite 3, Fig. 5a, Kelsey et
694 al. 2008). Core monazite from EH48 leucosome (Fig. 5a) may be equivalent to monazite (3) in
695 EH45 and EH49 (Fig 5c). A very thin (<5μm thick) zone of low Y between monazite (3) and
696 (4/5) on grain 45a4 (Fig. 5a) may represent a poorly preserved phase of retrograde monazite
697 growth or perhaps an irregular overgrowth pattern for monazite (3).
698 High Y monazite rims in sample EH49 (monazite 4–5) give either Latest Cretaceous (76–
699 68 Ma) or Eocene–Oligocene (42.2 ± 4.4 and 31.9 ± 4.8 Ma) ages. Xenotime is present in EH49
700 along the resorbed rims of garnet (Hallett and Spear 2014), and is inferred to have been in
701 equilibrium with matrix monazite (4) and/or (5). A monazite rim + xenotime temperature of 526
702 ± 25ºC (Table 1) may thus represent monazite growth after significant garnet breakdown either
703 (1) following melt crystallization (within ~15 m.y., monazite 4), or (2) during renewed heating
704 another 20–30 million years later (monazite 5). Due to a similar appearance and composition
705 among monazite (4) and (5), as well as poorly constrained and discordant U/Th–Pb ages, it is not
706 possible to meaningfully link monazite rim + xenotime temperatures to the P–T–t path.
707

708 **U/TH–PB AGES IN A PETROLOGIC CONTEXT**

U/Th–Pb ages are compiled for all samples in this study in Fig. 8. Zircon analyses from Winchell Lake nappe samples EH09–EH10 are interpreted to represent continuous or possibly episodic zircon growth during a period ranging from 58.9 ± 3.6 to 77.4 ± 12.4 Ma. EH09–EH10 zircon ages suggest some leucosome segregations may have crystallized by ~72 Ma whereas melanosome zircon growth shows a more evenly spread age distribution spanning ~18 million years. This observation may represent a protracted period of zircon growth or potentially unresolved episodic melt/zircon crystallization events. More melt was produced than the volume corresponding to the relatively sparse leucosomes, as a significant volume of melt was removed from this rock (Hallett and Spear 2014). If all of this zircon growth was during crystallization of partial melt that formed in situ, then leucosome crystallization may have been a long-lived event, or possibly several episodic events, suggesting relatively slow cooling near the effective solidus for this rock.

Initial monazite growth in the Winchell Lake nappe samples EH09–EH10 occurred during early prograde chlorite/garnet zone metamorphism, which was underway by 86.8 ± 5.6 Ma (the oldest EH10 monazite 1). This age is not recorded by monazite in sample EH21. Low Y monazite mantles in samples EH09–EH10, and low Y matrix monazite in sample EH21, are interpreted to have grown during melt crystallization, loosely constrained to have occurred between 59.9 ± 4.4 and 71.8 ± 4.0 Ma. High Y rims on most matrix grains from these samples represents renewed monazite growth 20–30 m.y. after melt crystallization.

Lizzies Basin block metapelite zircon (EH49) show distinct age ranges for the melanosome (81.1 ± 6.6, to 86.7 ± 13.4 Ma) and leucosome (61.4 ± 5.6 to 64.7 ± 3.7 Ma). This distinction could represent zircon growth on two different segments of the P–T path, or perhaps two melt crystallization events in the Lizzies Basin block. In consideration of the inferences from

732 monazite paragenesis discussed above, the melanosome ages are consistent with a period of melt
733 crystallization in these rocks. The leucosome zircon age, with the unique HREE inflection (Fig.
734 9c), is puzzling as it is younger than the youngest pre-Eocene monazite growth from samples
735 EH45, EH49, and EH48, which are interpreted to represent melt crystallization in the Lizzies
736 Basin block. EH49 Leucosome zircon is also younger than Winchell Lake nappe melt
737 crystallization dated by zircon and monazite. It is possible that these leucosome zircon ages are
738 mixtures with unrecognized, thin Tertiary rims. Another possibility is that this age could
739 represent retrograde recrystallization during reheating and continued metamorphism in the
740 Lizzies Basin block, as suggested for Eocene (~38 Ma) and Oligocene (~29 Ma) magmatism in
741 the Ruby Mountains (Howard et al. 2011).
742 Monazite from the Lizzies Basin block metapelites contains some relict, irregularly
743 shaped Jurassic to Early Cretaceous cores (e.g., monazite 1, Fig. 5a), giving ages between 157.6
744 ± 3.6 and 123.6 ± 12.4 Ma with younger ages possibly representing mixtures (e.g., EH45–EH49,
745 Fig. 5c). Late Cretaceous monazite core growth in Lizzies Basin block metapelites occurred
746 between 97.0 ± 9.2 and 76.5 ± 4.0 Ma, with discrete compositional zones resolvable in some
747 samples (EH45 and EH49 monazite 2 and 3, Fig. 5a) that are inferred to represent monazite
748 grown due to different metamorphic and/or melt crystallization reactions. Monazite cores from
749 leucosome sample EH48 are higher in Y, U, and Th than monazite of the host restitic schist
750 (samples EH45 and EH49; see Supplementary data). Whereas some EH48 grains do contain
751 small patches of lower Y that are too small for analysis, the high-Y cores are prevalent and the
752 prograde zoning seen in EH30, EH31, EH45, and EH49 is not present, suggesting that monazite
753 cores are of igneous origin. Therefore the leucosome (EH48) age of 80.1 ± 1.4 Ma is interpreted
754 to represent a phase of Lizzies Basin block in situ melt crystallization. Significantly, this age is

within the range of melanosome zircon ages from EH49 suggesting that melt crystallized at ~80 Ma in both units. Melanosome schist/gneiss samples EH30, EH31, EH45, and EH49 give age ranges for monazite compositional domains that span this leucosome (EH48) age and hence monazite growth during melt crystallization in these samples may not be resolved from prograde monazite growth ages.

High Y rims present on many Lizzies Basin block monazite grains probably represent growth during retrograde metamorphism driven by garnet breakdown and/or melt crystallization, possibly recording slight thermal pulses associated with igneous intrusion.

DISCUSSION AND IMPLICATIONS

The monazite and zircon ages presented above define the timing along segments of the P–T–t paths for the Winchell Lake nappe and the Lizzies Basin block (Fig. 13). The structural complexity of the Ruby Mountains–East Humboldt Range, in particular the Winchell Lake nappe (McGrew et al. 2000; Henry et al. 2011), makes interpretation of the metamorphic and tectonic history of these crustal blocks difficult. It is unclear whether Winchell Lake nappe emplacement entirely overprints peak-T metamorphism. It seems likely that nappe formation began under high grade metamorphic conditions, and continued during leucogranite intrusion concentrated along the lower limb.

The oldest group of Late Cretaceous ages in the Winchell Lake nappe and Lizzies Basin block metapelites of the East Humboldt Range are part of the ~ 82.9 ± 7.1 to 97.0 ± 9.2 Ma monazite (2–3) age range from EH45–EH49 (Fig. 8). Monazite–xenotime thermometry of exclusively monazite (2) from these samples yield temperatures of 420-470 ˚C representative of the conditions of greenschist facies sub-garnet grade metamorphism. The oldest group of

778 monazite ages in the Winchell Lake nappe (mean age: 82.8 ± 1.3 Ma, Fig. 8) similarly yields low
779 monazite–xenotime temperatures (380–450˚C). Comparison of the results from the Lizzies Basin
780 block and Winchell Lake nappe indicate that early prograde metamorphism was not synchronous
781 in the two tectonic units. Additionally, the lack of analyzed monazite of this Winchell Lake
782 nappe age range from the mylonitic paragneiss sample (EH21) may represent further complexity
783 in the metamorphic and structural evolution of the Winchell Lake nappe. Sample EH21 contains
784 monazite that appears as inclusions in garnet, potentially recording amphibolite facies monazite
785 growth during breakdown of allanite. Allanite, however, is not present, and such a monazite
786 forming reaction would have had to predate growth of poikiloblastic garnet. Further study is
787 needed to resolve the paragenesis of EH21 monazite cores in order to constrain whether this rock
788 shared the prograde P–T–t history of the graphitic schist EH09–EH10.
789 Differences in the Winchell Lake nappe and Lizzies Basin block prograde P–T paths
790 (Figs. 2, 13; and Hallett and Spear 2014) suggests these blocks reached different maximum
791 pressures and peak metamorphic conditions. In all Lizzies Basin block metapelite samples plus
792 the Winchell Lake nappe graphitic schist (EH09–EH10) monazite and zircon from the
793 amphibolite facies portion of the prograde path are apparently absent and the next recorded ages
794 are interpreted to reflect the onset of melt crystallization during cooling. In the Lizzies Basin
795 block, melanosome zircon ages of 81.1 ± 6.6 to 86.7 ± 13.4 Ma and leucosome monazite ages of
796 80.1 ± 1.4 Ma are generally older than zircon from the upper limb of the Winchell Lake nappe
797 (58.9 ± 3.6 to 77.4 ± 12.4 Ma). The interpretation that these Lizzies Basin block ages represent a
798 melt crystallization event implies that melting and subsequent crystallization began earlier in the
799 Lizzies Basin block (see Fig. 8). Monazite rim ages from the Lizzies Basin block of 74.4 ± 6.8 to
800 68.2 ± 4.7 Ma, in addition to zircon ages from a Lizzies Basin block leucosome of 65.9 ± 2.2 to

801 59.0 ± 1.2 Ma, suggest that retrograde recrystallization, or perhaps a late-stage melt
802 crystallization event, was experienced by these rocks (Fig. 8). Monazite ages from the Winchell
803 Lake nappe upper limb that are interpreted to be melt-related (59.9 ± 4.4 to 71.8 ± 4.0 Ma)
804 overlap monazite rim and leucosome zircon ages from the Lizzies Basin block (Fig. 8).
805 In the Winchell Lake nappe graphitic schist (EH09–EH10) the spread in monazite (1)
806 ages slightly overlaps the range in zircon ages. Present limitations regarding the precision of this
807 technique make interpretations of such datasets difficult. The monazite zoning, thermometry, and
808 theoretical modeling results suggest that monazite (1) growth occurred during greenschist facies
809 metamorphism and prior to any melting that occurred in these rocks. Taken together, the
810 monazite and zircon ages constrain peak metamorphism within the upper limb of the Winchell
811 Lake nappe to have occurred between the early prograde 82.8 ± 1.3 Ma monazite growth and
812 58.9 ± 3.6 to 77.4 ± 12.4 Ma, the range of melt crystallization ages. Only 5 of 17 zircon analyses
813 overlap the monazite (1) age within 2σ uncertainty. In the Lizzies Basin block, peak
814 metamorphism is poorly constrained by the data because of limited material (thin compositional
815 domains) for monazite grown during prograde metamorphism. However, early monazite core
816 growth likely falls within a range of 86.8 to 97.5 Ma (a 1σ envelope) for EH45–EH49 monazite
817 (2). Following burial and anatexis, the growth of melt-produced leucosome monazite at 80.1 ±
818 1.4 Ma is supported by several melanosome zircon analyses (EH49) consistent with this age.
819 These constraints suggest that Lizzies Basin block peak metamorphism generally pre-dates
820 constraints for peak metamorphism of the Winchell Lake nappe upper limb. Combining the
821 interpretation of different prograde histories for Winchell Lake nappe and Lizzies Basin block
822 rocks (Hallett and Spear 2014) with the U/Th–Pb geochronology presented here, the present
823 configuration of the Winchell Lake nappe and the Lizzies Basin block apparently was not in

place until after tectonic burial and partial decompression (and melting) of the upper limb of the Winchell Lake nappe had taken place.

Comparison with other regional ages

The earliest ages found in this study are the Jurassic monazite core ages of 147.5 ± 9.8 and 157.6 ± 3.6 Ma from EH31 (Fig. 5b), which are unique to Lizzies Basin block samples. These ages are similar to the time of intrusion of (1) the Dawley Canyon Granite in the central Ruby Mts. (Hudec and Wright 1990), dated by igneous monazite (153 ± 1 Ma), and (2) the Seitz Canyon Granodiorite (Howard et al. 2011) near Lamoille Canyon in the northern Ruby Mountains. These rocks intrude a similar stratigraphic level to, and are part of a deformed block that may be contiguous with, the Lizzies Basin block. The oldest ages (Jurassic to Early Cretaceous) from Lizzies Basin block samples EH45 and EH49 may be correlative, though possibly reflect some Pb loss.

An ID–TIMS U–Pb zircon age of 84.8 ± 2.8 Ma that used zircon fractions that were, "heavily abraded and carefully hand picked in order to avoid crystals with cores of premagmatic zircon," was published for a pegmatitic leucogranite from the nose of the Winchell Lake nappe (McGrew et al. 2000). McGrew et al. (2000) interpret this leucogranite as derived from anatexis of the migmatitic graphite schist, and zircons dated by SHRIMP in this study are from the same unit (melanosome and in situ leucosome, samples EH09–EH10) roughly 1.75 km away. The SHRIMP results from EH09–EH10 show no evidence of pre 78 Ma growth apart from detrital cores. This 84.8 ± 2.8 Ma age does match the 82.8 ± 1.3 Ma age determined for monazite (1) from EH09–EH10, though petrologic considerations indicate that this monazite age represents prograde growth at conditions below the garnet isograd, prior to anatexis and subsequent zircon

847 crystallization. Therefore, the TIMS age may be (1) an intrusive age for pegmatitic leucogranite,
848 suggesting that leucogranite intrusion was underway during the early stages of metamorphism
849 recorded in the Winchell Lake nappe samples, (2) a mixture of core + rim material, or (3)
850 crystallization of leucosomes formed by anatexis that was localized near the present day
851 Winchell Lake nappe axis, and potentially on the lower limb, and did not affect samples EH09–
852 EH10. McGrew et al. (2000) describe a field relationship where the dated leucogranite is folded
853 around the nose of the Winchell Lake nappe itself, noting that nappe formation and emplacement
854 must therefore postdate leucogranite crystallization. If the leucogranite was not locally derived
855 and the intrusive interpretation is correct, leucogranite intrusion may have influenced the thermal
856 structure of the Winchell Lake nappe at this time. An in situ anatectic origin to the zircon dated
857 by McGrew could indicate strong, localized advection of heat (and fluid?) by intrusive
858 magmatism at this time, forcing localized melting of the pelitic schist.
859 Zircon rim ages from Archean–Paleoproterozoic Angel Lake orthogneiss in the core of
860 the Winchell Lake nappe range from ~91–72 Ma (Premo et al. 2008, 2010). These ages overlap
861 with the EH09–EH10 zircon rim ages presented here, though part of the orthogneiss age range is
862 significantly older. In consideration of the petrologic constraints presented here, the full
863 "assembly" of the Winchell Lake nappe appears to post-date the greenschist facies monazite
864 growth in the upper limb, and hence anatexis and leucosome crystallization in Winchell Lake
865 nappe's Archean–Paleoproterozoic core probably occurred while these units were separated,
866 though their juxtaposition may have played a role in heating and migmatization of the upper limb
867 section. A syn-metamorphic Winchell Lake nappe "assembly", in contrast to the pre-
868 metamorphic fault (see Fig. 1) interpretation of McGrew et al. (2000), could explain the variation
869 in zircon crystallization ages discussed above. Such a scenario would include potential

differences in the metamorphic evolution between Winchell Lake nappe upper limb (EH09–EH10) and core (EH21) rocks.

Regardless of the complex structural assembly of the Winchell Lake nappe block, high Y monazite rims giving Eocene–Oligocene (30–40 Ma) $^{206}Pb/^{238}U$ ages are found in both the Winchell Lake nappe and Lizzies Basin block. These ages are interpreted to represent a heating and/or fluid event at this time based on monazite + xenotime thermometry. Eocene–Oligocene zircon growth is revealed by SIMS geochronology from migmatitic paragneisses in the lower limb of the Winchell Lake nappe (Metcalf and Drew 2011) and in pegmatitic leucogranites from the structurally deepest portions of the Ruby Mountains (Howard et al. 2011). These authors suggest that these zircon ages represent persistence of, or remelting/crystallization of, anatectic melts at this time. This Eocene–Oligocene zircon growth in the lower limb of the Winchell Lake nappe (Metcalf and Drew 2011) may be related to the heating/fluid event that produced high Y rims on monazite. The 3 youngest (leucosome) zircon rim analyses from Lizzies Basin block sample EH49 yield concordant Paleocene SHRIMP ^{207}Pb-corrected $^{206}Pb/^{238}U$ ages from 61.4 ± 5.6 to 64.7 ± 3.7 Ma, and the youngest zircon from Winchell Lake nappe samples EH09–EH10 is 58.9 ± 3.6 Ma. On this basis, it is apparent that in situ partial melt had completely crystallized in the East Humboldt Range by ~55 Ma. No younger (Eocene–Oligocene) zircon was found in the samples for this study, though depth profiling of separated zircon grains (e.g., Gordon et al. 2009) was not performed.

Constraints on the early exhumation and thermal history of the Ruby Mountains–East Humboldt Range

892 The geochronologic data presented here, when linked with P–T histories presented in
893 Hallett and Spear (2014), provide constraints on the absolute timing and estimates of the rates of
894 burial and exhumation. Geochronologic constraints used for the ranges of burial and exhumation
895 rates are the same and represent a cycle of both burial and exhumation. Therefore the minimum
896 estimates are strongly conservative and could only have been approached when coupled with
897 extremely rapid deformation and/or erosion. Calculated burial, exhumation, heating, and cooling
898 rates are presented as maxima and minima in Tables 2 and 3. The significantly higher upper end
899 of the burial rates for the Winchell Lake nappe upper limb rocks vs. the Lizzies Basin block
900 burial rates reflect the tectonic loading discussed by Hallett and Spear (2014).
901 Rates are presented for episodic exhumation events that acted to emplace high-grade
902 metamorphic rocks into a shallower level in the middle crust. As discussed above, discrete
903 accommodating structures for this phase of exhumation are presently unexposed/unknown.
904 Exhumation may therefore have been in part accommodated by ductile thinning and/or focused
905 erosion in place of or in addition to discrete shearing/faulting. Nonetheless, these exhumation
906 events set the stage for the strongly overprinting "core complex" phase of exhumation, facilitated
907 by top to the WNW ductile shearing across the Ruby Mountains–East Humboldt Range (see
908 McGrew and Snee 1994; Colgan et al. 2010).
909 For the upper limb of the Winchell Lake nappe, estimates of the rates of
910 heating/exhumation/cooling were calculated by taking the timing of monazite (1) growth
911 interpreted to represent greenschist facies metamorphism below the garnet isograd in samples
912 EH09–EH10 with zircon ages from the same samples interpreted to represent crystallization of
913 melt formed in situ. Petrologic considerations suggest as much as 7 kbar of compression
914 followed by ~3–4 kbar of decompression occurred between these accessory mineral growth

915 events, coupled with ~200º of heating and ~60º of subsequent cooling (Hallett and Spear 2014).
916 Exhumation by non-vertical structures alone would require slip rates that are faster than these
917 exhumation rate estimates by a factor of 1/sin θ, where θ is the down-dip slip component of the
918 corresponding structure.

919 Constraining the exhumation of the Lizzies Basin block is less straightforward because of
920 difficulties linking accessory mineral growth to the P–T path (see "Yttrium thermometry and
921 monazite paragenesis" above). Using U–Pb SHRIMP ages from EH45–EH49 monazite (2),
922 which was used for monazite + xenotime thermometry, gives only a rough estimate of the timing
923 for early greenschist facies metamorphism due to a small number of ages (n=4) in this
924 volumetrically minor domain, and therefore the rates of subsequent burial, heating, and
925 exhumation are presented with caution. Petrologic considerations suggest the Lizzies Basin block
926 was subject to ~3 kbar of compression and ~300º of heating, followed by and 2–3 kbar of
927 decompression and ~200º of cooling prior to the core complex phase of exhumation.

928 The exhumation rates presented here (Table 2) are generally at the low end for
929 exhumation by extensional "core complex" deformation catalogued by Bendick and Baldwin
930 (2009) for metamorphic core complexes north of the Snake River Plain, which fall between ~1.5
931 and 6.0 km/m.y. Note that the exhumation rates from Bendick and Baldwin (2009) are mean
932 values based in most cases on broad barometric constraints and different thermochronometers. In
933 addition, the initial exhumation phase presented here is interpreted to pre-date core complex
934 extensional deformation and, as noted above and in the literature (e.g. Hodges et al. 1992;
935 McGrew et al. 2000; Hallett and Spear 2014), lacks a clear mechanism or exposed
936 accommodating structure. For comparison, the footwall of the Wasatch fault, a large-scale
937 notably active normal fault in central Utah, gives an average exhumation rate of 0.3–0.6 km/m.y.

938 since 10–15 Ma (Nelson et al. 2009). It appears likely that the exhumation pulses recorded by the
939 studied samples were not accommodated exclusively by normal sense shearing, and that focused
940 erosion and/or ductile thinning played a significant role. Exhumation mechanisms of high-grade
941 metamorphic rocks via ductile thinning are the subject of much debate with models ranging from
942 subvertical diapiric rise of orogenic crust (e.g. Whitney et al. 2004) to ductile extrusion via a low
943 viscosity crustal channel coupled with erosion (e.g. Beaumont et al. 2001). Evidence pointing to
944 which process or processes may have been responsible for the early phases of exhumation in the
945 Ruby Mountains–East Humboldt Range is inconclusive and obscured structural complexity,
946 magmatism, and limited exposure.

947 In addition, heating and cooling rates are presented in Table 3. Heating rates for the
948 Winchell Lake nappe upper limb are somewhat higher than those for the Lizzies Basin block.
949 This may be a result of a larger degree of heat advection by intrusive magmatism in the Winchell
950 Lake nappe prior to juxtaposition of the two blocks. Relatively slow average cooling rates may
951 obscure more rapid initial cooling of the Winchell Lake nappe during exhumation, evidenced by
952 partially preserved garnet major element zoning patterns (Hallett and Spear 2014).

953

954 **The presence and significance of partial melt**

955 In situ partial melting is interpreted to have occurred in the Lizzies Basin block as a
956 consequence of regional metamorphism, prior to any exhumation or decompression, whereas
957 partial melting of the Winchell Lake nappe, as recorded in the upper limb, occurred after
958 decompression had begun (see Hallett and Spear 2014). The absolute timing of the onset of
959 anatexis is unfortunately not recorded in the geochronometers examined. Evidence for partial
960 melting and petrologic considerations indicate melt was present for a portion of the initial

961 exhumation phase of the Winchell Lake nappe upper limb rocks, and for portions of both the
962 burial and exhumation phases of the Lizzies Basin block. While estimated exhumation rates may
963 not be as high as some extensional metamorphic core complexes, this exhumation is still quite
964 significant when integrated over 5–21 m.y. It is feasible that these average rates obscure a faster
965 episode(s) of exhumation during a period(s) when distributed partial melt was present in the
966 system affecting rock strength.

967 These constraints on the residence time of in situ melt in both the Lizzies Basin block and
968 the Winchell Lake nappe are rather broad, leaving the possibility of prolonged melt
969 crystallization in the lower crust, with progress recorded by continued monazite and zircon
970 crystallization. It is however possible that in situ melting and melt crystallization in most
971 metapelites occurred as an unresolved (series of) short-lived event(s) during decompression
972 giving way to cooling (Fig. 13a). A third plausible scenario is that regional melt fluxes, mixing
973 with or supplanting in situ-formed melt, contributed to the growth of zircon and yielded diverse
974 trace element concentrations in melanosome zircon. This zircon could have grown during
975 periods of small volume pegmatitic melt flux and advection of heat, tracking changes in the melt
976 source region through the Late Cretaceous. This is proposed for leucogranites of the Ruby
977 Mountains based on decreasing zircon εHf values with age (Romanoski et al. 2012). Resolution
978 of this conundrum must await further high precision geochronologic and geochemical study.

979 The cause of Late Cretaceous decompression and melting recorded in the Winchell Lake
980 nappe is unclear, but may be related to lithospheric mantle delamination (Wells and Hoisch
981 2008), buoyant diapiric rise of deep crust (e.g. Whitney et al. 2004), and/or some other
982 "external" driving force (McGrew et al. 2000). Regardless, the presence of melt in the Winchell
983 Lake nappe and Lizzies Basin block at this time may have acted to enhance ductile flow,

984 effectively "weakening" these crustal blocks and allowing tectonic forces to emplace them into a
985 shallower crustal level. Penetrative deformation and ductile flow of these blocks occurred in the
986 middle crust, possibly with advection of heat associated with intrusions such as the ~69 Ma two-
987 mica leucogranites of the Ruby Mountains (Howard et al. 2011). These changes to the thermal
988 structure at this time, if accompanied by an influx of fluid, could have caused the Lizzies Basin
989 block to re-cross the pelite solidus and produce small amounts of anatectic melt from which 76–
990 68 Ma monazite rims (monazite 4, EH45 and EH49), and possibly leucosome zircon rims (?),
991 crystallized.
992
993 **CONCLUDING REMARKS**
994 In situ monazite and zircon U/Th–Pb dating in conjunction with accessory mineral / trace
995 element thermometry, garnet zoning analysis, and theoretical modeling provides insights into the
996 metamorphic and partial melting history of different crustal blocks from the thickened hinterland
997 of the Sevier orogenic belt. Both the Lizzies Basin block and the Winchell Lake nappe
998 underwent burial and migmatization, but differences in the timing constraints for prograde garnet
999 zone metamorphism (monazite), early exhumation and cooling (monazite and zircon), plus
1000 differences in the peak pressures and temperatures (Hallett and Spear 2014), result from a
1001 tectonic reconfiguration of these crustal blocks that apparently occurred during and/or after early
1002 exhumation but prior to the strongly overprinting core complex phase of exhumation.
1003 Constraints on exhumation rates based on the high-grade portions of the Pressure–
1004 Temperature–time histories presented here suggest that following rapid tectonic burial of upper
1005 limb rocks of the Winchell Lake nappe, exhumation occurred at rates generally between those
1006 for Cordilleran metamorphic core complexes north of the Snake River Plain (where exhumation

is attributed in part to ductile thinning and erosion, Bendick and Baldwin 2009) and exhumation by large scale brittle normal faulting, with overlap of uncertainties with rates for both mechanisms. We infer that large scale normal faulting of the upper crust alone probably could not have resulted in the exhumation rates calculated by this technique, particularly for the Winchell Lake nappe. Episodic Late Cretaceous exhumation in this part of the North American Cordillera therefore apparently involved a degree of ductile thinning/erosion. The presence or the formation of in situ partial melt during episodic exhumation probably had a significant effect on the rheological properties of these crustal blocks. Our results demonstrate how combining monazite and zircon in situ geochronology with petrologic observations and theoretical modeling can provide important information about the assembly, melting history, and early exhumation of complexly thickened orogenic crust.

ACKNOWLEDGEMENTS

The authors thank J. Wooden for help with sample preparation and SHRIMP analysis, J. Price and D. Ruscitto for assistance with the electron microprobe and the Corman Center for Mass Spectrometry (LA–ICPMS). Thorough, constructive reviews by I. Fitzsimmons, E. Gottlieb, and anonymous reviewers greatly improved this manuscript. The authors also thank C. Hetherington and G. Dumond for editorial handling of the manuscript. This research was funded by NSF grants EAR-1019768, EAR-0337413, and EAR-0409622 to F.S.S., the Edward P. Hamilton Distinguished Chair for Science Education, and a graduate student research grant from the Geological Society of America.

REFERENCES CITED

1030 Aleinikoff, J.N., Schenck, W.S., Plank, M.O., Srogi, L.A., Fanning, C.M., Kamo, S.L., and
1031 Bosbyshell, H. (2006) Deciphering igneous and metamorphic events in high-grade rocks
1032 of the Wilmington Complex, Delaware: Morphology, cathodoluminescence and
1033 backscattered electron zoning, and SHRIMP U-Pb geochronology of zircon and
1034 monazite. Geological Society of America Bulletin, 118, 39–64.
1035 Anders, E., and Grevesse, N. (1989) Abundances of the elements: Meteoritic and solar.
1036 Geochimica et Cosmochimica Acta, 53, 197–214.
1037 Armstrong, R.L., and Ward, P. (1991) Evolving geographic patterns of Cenozoic magmatism in
1038 the North American Cordillera: The temporal and spatial association of magmatism and
1039 metamorphic core complexes. Journal of Geophysical Research: Solid Earth, 96, 13201–
1040 13224.
1041 Barth, A.P., and Wooden, J.L. (2010) Coupled elemental and isotopic analyses of polygenetic
1042 zircons from granitic rocks by ion microprobe, with implications for melt evolution and
1043 the sources of granitic magmas. Chemical Geology, 277, 149–159.
1044 Batum, M.A. (1999) Petrology of Late Cretaceous and Cenozoic granitic rocks, East Humboldt
1045 Range, 167 p. M.S. thesis, Texas Tech University, Lubbock.
1046 Beaumont, C., Jamieson, R.A., Nguyen, M.H., and Lee, B. (2001) Himalayan tectonics
1047 explained by extrusion of a low-viscosity crustal channel coupled to focused surface
1048 denudation. Nature, 414, 738–742.
1049 Bendick, R., and Baldwin, J. (2009) Dynamic models for metamorphic core complex formation
1050 and scaling: The role of unchannelized collapse of thickened continental crust.
1051 Tectonophysics, 477, 93–101.

1052 Colgan, J.P., Howard, K.A., Fleck, R.J., and Wooden, J.L. (2010) Rapid middle Miocene
1053 extension and unroofing of the southern Ruby Mountains, Nevada. Tectonics, 29,
1054 TC6022.
1055 Coney, P.J., and Harms, T.A. (1984) Cordilleran metamorphic core complexes: Cenozoic
1056 extensional relics of Mesozoic compression. Geology, 12, 550–553.
1057 Corfu, F., Hanchar, J.M., Hoskin, P.W.O., and Kinny, P. (2003) Atlas of zircon textures. In J.M.
1058 Hanchar and P.W.O. Hoskin, Eds., Zircon, 53, p. 469–500. Reviews in Mineralogy and
1059 Geochemistry, Mineralogical Society of America, Washington D.C.
1060 Corrie, S.L., and Kohn, M.J. (2008) Trace-element distributions in silicates during prograde
1061 metamorphic reactions: implications for monazite formation. Journal of Metamorphic
1062 Geology, 26, 451–464.
1063 Coryell, C.D., Chase, J.W., and Winchester, J.W. (1963) A procedure for geochemical
1064 interpretation of terrestrial rare-earth abundance patterns. Journal of Geophysical
1065 Research, 68, 559–566.
1066 Dallmeyer, R.D., Snoke, A.W., and McKee, E.H. (1986) The Mesozoic-Cenozoic tectonothermal
1067 evolution of the Ruby Mountains, East Humboldt Range, Nevada: A Cordilleran
1068 metamorphic core complex. Tectonics, 5, 931–954.
1069 Daniel, C.G., and Pyle, J.M. (2006) Monazite–Xenotime thermochronometry and Al_2SiO_5
1070 reaction textures in the Picuris Range, Northern New Mexico, USA: new evidence for a
1071 1450–1400 Ma orogenic event. Journal of Petrology, 47, 97–118.
1072 Dempster, T.J., Hay, D.C., Gordon, S.H., and Kelly, N.M. (2008) Micro-zircon: origin and
1073 evolution during metamorphism. Journal of Metamorphic Geology, 26, 499–507.

1074 Dokka, R.K., Mahaffie, M.J., and Snoke, A.W. (1986) Thermochronologic evidence of major
1075 tectonic denudation associated with detachment faulting, northern Ruby Mountains-East
1076 Humboldt Range, Nevada. Tectonics, 5, 995–1006.
1077 Ferry, J.M., and Watson, E.B. (2007) New thermodynamic models and revised calibrations for
1078 the Ti-in-zircon and Zr-in-rutile thermometers. Contributions to Mineralogy and
1079 Petrology, 154, 429–437.
1080 Foster, G., Parrish, R.R., Horstwood, M.S.A., Chenery, S., Pyle, J., and Gibson, H. (2004) The
1081 generation of prograde PTt points and paths; a textural, compositional, and chronological
1082 study of metamorphic monazite. Earth and Planetary Science Letters, 228, 125–142.
1083 Fu, B., Page, F.Z., Cavosie, A.J., Fournelle, J., Kita, N.T., Lackey, J.S., Wilde, S.A., and Valley,
1084 J.W. (2008) Ti-in-zircon thermometry: applications and limitations. Contributions to
1085 Mineralogy and Petrology, 156, 197–215.
1086 Gordon, S.M., Grove, M., Whitney, D.L., Schmitt, A.K., and Teyssier, C. (2009) Time-
1087 temperature-fluid evolution of migmatite dome crystallization: coupled U-Pb age, Ti
1088 thermometry, and O isotopic ion microprobe depth profiling of zircon and monazite.
1089 Chemical Geology, 262, 186–201.
1090 Gratz, R., and Heinrich, W. (1997) Monazite-xenotime thermobarometry: Experimental
1091 calibration of the miscibility gap in the binary system $CePO_4$-YPO_4. American
1092 Mineralogist, 82, 772–780.
1093 Hallett, B.W., and Spear, F.S. (2014) The P–T history of anatectic pelites of the northern East
1094 Humboldt Range, Nevada: Evidence for tectonic loading, decompression, and anatexis.
1095 Journal of Petrology, 55, 3–36.

1096 Harley, S.L., and Kelly, N.M. (2007) The impact of zircon–garnet REE distribution data on the
1097 interpretation of zircon U–Pb ages in complex high-grade terrains: An example from the
1098 Rauer Islands, East Antarctica. Chemical Geology, 241, 62–87.
1099 Henry, C.D., McGrew, A.J., Colgan, J.P., Snoke, A.W., and Brueseke, M.E. (2011) Timing,
1100 distribution, amount, and style of Cenozoic extension in the northern Great Basin.
1101 Geological Society of America Field Guide, 21, 27–66.
1102 Hinchey, A.M., Carr, S.D., McNeill, P.D., and Rayner, N. (2006) Paleocene-Eocene high-grade
1103 metamorphism, anatexis, and deformation in the Thor-Odin dome, Monashee complex,
1104 southeastern British Columbia. Canadian Journal of Earth Sciences, 43, 1341–1365.
1105 Hoskin, P., and Black, L. (2000) Metamorphic zircon formation by solid-state recrystallization of
1106 protolith igneous zircon. Journal of Metamorphic Geology, 18, 423–439.
1107 Hoskin, P.W.O., and Schaltegger, U. (2003) The composition of zircon and igneous and
1108 metamorphic petrogenesis. In J.M. Hanchar and P.W.O. Hoskin, Eds., Zircon, 53, p. 27–
1109 62. Reviews in Mineralogy and Geochemistry, Mineralogical Society of America,
1110 Washington D.C.
1111 Howard, K.A., Kistler, R.W., Snoke, A.W., and Willden, R. (1979) Geologic map of the Ruby
1112 Mountains, Nevada. United States Geological Survey, Map I-1136.
1113 Howard, K.A., Wooden, J.L., Barnes, C.G., Premo, W.R., Snoke, A.W., and Lee, S.Y. (2011)
1114 Episodic growth of a Late Cretaceous and Paleogene intrusive complex of pegmatitic
1115 leucogranite, Ruby Mountains core complex, Nevada, USA. Geosphere, 7, 1220–1248.
1116 Hudec, M., and Wright, J. (1990) Mesozoic history of the central part of the Ruby Mountains–
1117 East Humboldt Range metamorphic core complex. Nevada. Geological Society of
1118 America Abstracts with Programs, 22, 30.

1119 Kelly, N.M., Clarke, G.L., and Harley, S.L. (2006) Monazite behaviour and age significance in
1120 poly-metamorphic high-grade terrains: A case study from the western Musgrave Block,
1121 central Australia. Lithos, 88, 100–134.
1122 Kelsey, D.E., Clark, C., and Hand, M. (2008) Thermobarometric modelling of zircon and
1123 monazite growth in melt-bearing systems: examples using model metapelitic and
1124 metapsammitic granulites. Journal of Metamorphic Geology, 26, 199–212.
1125 Kistler, R.W., Ghent, E.D., and O'Neil, J.R. (1981) Petrogenesis of garnet two-mica granites in
1126 the Ruby Mountains, Nevada. Journal of Geophysical Research, 86, 10591–10606.
1127 Kretz, R. (1983) Symbols for rock-forming minerals. American Mineralogist, 68, 277–279.
1128 Kohn, M.J., Wieland, M.S., Parkinson, C.D., and Upreti, B.N. (2005) Five generations of
1129 monazite in Langtang gneisses: implications for chronology of the Himalayan
1130 metamorphic core. Journal of Metamorphic Geology, 23, 399–406.
1131 Lee, S., Barnes, C.G., Snoke, A.W., Howard, K.A., and Frost, C.D. (2003) Petrogenesis of
1132 Mesozoic, peraluminous granites in the Lamoille Canyon area, Ruby Mountains, Nevada,
1133 USA. Journal of Petrology, 44, 713–732.
1134 Ludwig, K.R. (2003) Isoplot 3.00: A geochronological toolkit for Microsoft Excel. Berkeley
1135 Geochronology Center, Special Publication 4, 70p.
1136 Ludwig, K.R. (2009) Squid 2: A User's Manual, rev. 12 Apr 2009. Berkeley Geochronology
1137 Center, Special Publication 5, 110p.
1138 Lush, A.P., McGrew, A.J., Snoke, A.W., and Wright, J.E. (1988) Allochthonous Archean
1139 basement in the northern East Humboldt Range, Nevada. Geology, 16, 349–353.

1140 McGrew, A.J., and Premo, W.R. (2011) The Angel Lake gneiss complex of northeastern Nevada
1141 and the southwestern limits of Archean to Paleoproterozoic basement in North America.
1142 Geological Society of America Abstracts with Programs, 43, 435.
1143 McGrew, A.J., and Snee, L.W. (1994) $^{40}Ar/^{39}Ar$ thermochronologic constraints on the
1144 tectonothermal evolution of the Northern East Humboldt range metamorphic core
1145 complex, Nevada. Tectonophysics, 238, 425–450.
1146 McGrew, A.J., and Snoke, A.W. (2010) SHRIMP-RG U-Pb isotopic systematics of zircon from
1147 the Angel Lake Orthogneiss, East Humboldt Range, Nevada; is this really Archean
1148 crust?; discussion. Geosphere, 6, 962–965.
1149 McGrew, A.J., Peters, M.T., and Wright, J.E. (2000) Thermobarometric constraints on the
1150 tectonothermal evolution of the East Humboldt Range metamorphic core complex,
1151 Nevada. Geological Society of America Bulletin, 112, 45–60.
1152 Metcalf, R.V., and Drew, J. (2011) Cretaceous and Eocene-Oligocene U–Pb Zircon Migmatite
1153 Ages from the East Humboldt Range Metamorphic Core Complex, Nevada. Geological
1154 Society of America Abstracts with Programs, 43, 275.
1155 Nelson, S.T., Harris, R.A., Kowallis, B.J., Dorais, M., Constenius, K.N., Heizler, M., Barnett, D.
1156 (2009) The long-term burial and exhumation history of basement blocks in the footwall
1157 of the Wasatch fault, Utah. Rocky Mountain Geology, 44, 103–119.
1158 Norlander, B.H., Whitney, D.L., Teyssier, C., and Vanderhaeghe, O. (2002) Partial melting and
1159 decompression of the Thor-Odin dome, Shuswap metamorphic core complex, Canadian
1160 Cordillera. Lithos, 61, 103–125.
1161 Pitzer, K.S., and Sterner, S.M. (1994) Equations of state valid continuously from zero to extreme
1162 pressures for H_2O and CO_2. Journal of Chemical Physics, 101, 3111–3116.

1163 Premo, W.R., Howard, K.A., and Castiñeiras, P. (2005) New Shrimp U-Pb zircon ages and Nd
1164 isotopic signatures for plutonism in the Northern Ruby-East Humboldt Ranges of NE
1165 Nevada: Implications for the timing of Tertiary core complex formation. Geological
1166 Society of America Abstracts with Programs, 37, 359.
1167 Premo, W.R., Castiñeiras, P., and Wooden, J.L. (2008) SHRIMP-RG U-Pb isotopic systematics
1168 of zircon from the Angel Lake orthogneiss, East Humboldt Range, Nevada: Is this really
1169 Archean crust? Geosphere, 4, 963–975.
1170 Premo, W.R., Castiñeiras, P., and Wooden, J.L. (2010) SHRIMP-RG U-Pb isotopic systematics
1171 of zircon from the Angel Lake Orthogneiss, East Humboldt Range, Nevada; is this really
1172 Archean crust?; reply. Geosphere, 6, 966–972.
1173 Pyle, J.M., and Spear, F.S. (1999) Yttrium zoning in garnet: coupling of major and accessory
1174 phases during metamorphic reactions. Geological Materials Research, 1, 1–49.
1175 Pyle, J.M., and Spear, F.S. (2000) An empirical garnet (YAG)–xenotime thermometer.
1176 Contributions to Mineralogy and Petrology, 138, 51–58.
1177 Pyle, J.M., and Spear, F.S. (2003) Four generations of accessory-phase growth in low-pressure
1178 migmatites from SW New Hampshire. American Mineralogist, 88, 338–351.
1179 Pyle, J.M., Spear, F.S., Rudnick, R.L., and McDonough, W.F. (2001) Monazite–xenotime–
1180 garnet equilibrium in metapelites and a new monazite–garnet thermometer. Journal of
1181 Petrology, 42, 2083–2107.
1182 Pyle, J.M., Spear, F.S., and Wark, D.A. (2002) Electron microprobe analysis of REE in apatite,
1183 monazite and xenotime: protocols and pitfalls. In M.J. Kohn, J. Rakovan, and J.M.
1184 Hughes, Eds., Phosphates: Geochemical, Geobiological, and Materials Importance, 48, p.

337–362. Reviews in Mineralogy and Geochemistry, Mineralogical Society of America, Washington D.C.

Pyle, J.M., Spear, F.S., Cheney, J.T., and Layne, G. (2005) Monazite ages in the Chesham Pond Nappe, SW New Hampshire, USA: Implications for assembly of central New England thrust sheets. American Mineralogist, 90, 592–606.

Romanoski, A.M., Hetherington, C.J., Arendale, A.H., Barnes, C.G., and Cottle, J.M. (2012) Isotopic Evidence for Channel Flow Driven Lower Crustal Refertilization Beneath the Ruby Mountain–East Humboldt Metamorphic Core Complex. Geological Society of America Abstracts with Programs, 44, 129.

Rosenberg, C., and Handy, M. (2005) Experimental deformation of partially melted granite revisited: implications for the continental crust. Journal of Metamorphic Geology, 23, 19–28.

Rubatto, D. (2002) Zircon trace element geochemistry: partitioning with garnet and the link between U–Pb ages and metamorphism. Chemical Geology, 184, 123–138.

Schaltegger, U., Fanning, C., Günther, D., Maurin, J., Schulmann, K., and Gebauer, D. (1999) Growth, annealing and recrystallization of zircon and preservation of monazite in high-grade metamorphism: conventional and in-situ U-Pb isotope, cathodoluminescence and microchemical evidence. Contributions to Mineralogy and Petrology, 134, 186–201.

Snoke, A., McKee, E., and Stern, T. (1979) Plutonic, metamorphic, and structural chronology in the northern Ruby Mountains. Nevada: A preliminary report: Geological Society of America Abstracts with Programs, 11, 520–521.

Snoke, A.W., and Lush, A.P. (1984) Polyphase Mesozoic-Cenozoic deformational history of the northern Ruby Mountains-East Humboldt Range, Nevada. In Lintz, J. Ed., Western

Geological Excursions (Geological Society of America 1984 annual meeting field trip guidebook), v. 4, p. 232–260, Mackay School of Mines, Reno, Nevada.

Spear, F.S. (2004) Fast cooling and exhumation of the Valhalla metamorphic core complex, southeastern British Columbia. International Geology Review, 46, 193–209.

Spear, F.S. (2010) Monazite-allanite phase relations in metapelites. Chemical Geology, 279, 55–62.

Spear, F.S., and Pyle, J.M. (2010) Theoretical modeling of monazite growth in a low-Ca metapelite. Chemical Geology, 273, 111–119.

Sterner, S.M., and Pitzer, K.S. (1994) An equation of state for carbon dioxide valid from zero to extreme pressures. Contributions to Mineralogy and Petrology, 117, 362–374.

Teyssier, C., Ferré, E.C., Whitney, D.L., Norlander, B., Vanderhaeghe, O., and Parkinson, D. (2005) Flow of partially molten crust and origin of detachments during collapse of the Cordilleran orogen. In D. Bruhn and L. Burlini, Eds., High strain zones: Structure and physical properties, p. 39–64. Geological Society Special Publication 245, Geological Society of London.

Watson, E., Wark, D., and Thomas, J. (2006) Crystallization thermometers for zircon and rutile. Contributions to Mineralogy and Petrology, 151, 413–433.

Wells, M.L., and Hoisch, T.D. (2008) The role of mantle delamination in widespread Late Cretaceous extension and magmatism in the Cordilleran orogen, western United States. Geological Society of America Bulletin, 120, 515–530.

Whitehouse, M.J., and Kamber, B.S. (2003) A rare earth element study of complex zircons from early Archaean Amîtsoq gneisses, Godthåbsfjord, south-west Greenland. Precambrian Research, 126, 363–377.

Whitehouse, M.J., and Platt, J.P. (2003) Dating high-grade metamorphism–constraints from rare-earth elements in zircon and garnet. Contributions to Mineralogy and Petrology, 145, 61–74.

Whitney, D.L., Teyssier, C., and Fayon, A.K. (2004) Isothermal decompression, partial melting and exhumation of deep continental crust. In J. Grocott, K.J.W. McCafrey, G. Taylor, and B. Tikoff, Eds., Vertical coupling and decoupling in the lithosphere, p. 313–326, Geological Society Special Publication 227, Geological Society of London.

Wright, J.E., and Snoke, A.W. (1993) Tertiary magmatism and mylonitization in the Ruby-East Humboldt metamorphic core complex, northeastern Nevada: U-Pb geochronology and Sr, Nd, and Pb isotope geochemistry. Geological Society of America Bulletin, 105, 935–952.

FIGURE CAPTIONS

Figure 1. Geologic maps of portions of the northern East Humboldt Range showing locations of samples discussed in the text, after McGrew et al. (2000). (a) Location map showing Ruby Mountains–East Humboldt Range metamorphic core complex in gray. RM = Ruby Mountains, EHR = East Humboldt Range. (b) Northern map, covering the Winchell Lake nappe (WLN). The mapped pre-metamorphic fault of the Winchell Lake nappe (McGrew et al. 2000) separates Archean–Paleoproterozoic gneisses from Neoproterozoic–Paleozoic metasedimentary rocks. (c) Southern map, covering Lizzies/Weeks Basin area of the Lizzies Basin block (LBB).

Figure 2. P–T paths from the Winchell Lake nappe and Lizzies Basin block with thermobarometric constraints as in Hallett and Spear (2014), their figure 13. For full discussion see Hallett and Spear (2014). (a) Results from the Winchell Lake nappe with inferred P–T path. (b) Results form Lizzies Basin block with inferred P–T path.

Figure 3. Accessory mineral context from Ruby Mountains–East Humboldt Range metapelites. Abbreviations are lower case versions of Kretz (1983). White stars are locations of analyzed zircons; gray stars are analyzed monazites. (a) Cut slab from Winchell Lake nappe migmatitic graphite schist sample EH10 showing leucosome and melanosome domains. (b) Scan of thin section (EH10c-p) from rectangle in (a). Inset is plane polarized light photomicrograph of zircon 10c1 from biotite + sillimanite bearing leucosome. Location indicated by left rectangle shown in (b). (c) Cut slab from sample EH49 showing leucosome and melanosome domains. (d) Scan of thin section (EH49a-p) from rectangle in (c).

Figure 4. Monazite results from Winchell Lake nappe metapelitic rocks. (a) Representative Y X-ray maps of monazite from sample EH10 (top) and EH21 (bottom) showing location of SHRIMP analyses (white rings) with ^{207}Pb-corrected ^{206}Pb/^{238}U ages given. Small numbers in parentheses indicate interpreted growth domains. White dots and labels indicate monazite X_{Y+HREE} composition as determined by electron microprobe analysis. (b–c) Tera–Wasserburg plots of uncorrected monazite isotope ratios for Winchell Lake nappe samples (b) EH09–EH10 and (c) EH21, plotted with 2σ error ellipses. Interpreted growth domains correspond with numbers shown in parentheses in (a). Insets show full range of data with main plot area shown as black rectangle.

Figure 5. Monazite results from Lizzies Basin block metapelites and leucosomes. (a) Representative Y, U, and Th X-ray maps of monazite from samples EH30–EH31 (top) EH45–RH49 (middle) and EH48 (bottom) showing location of SHRIMP analyses (white rings) with ^{207}Pb-corrected ^{206}Pb/^{238}U ages given. Small numbers in parentheses indicate interpreted growth domains. White dots and labels indicate coffinite (X_{USiO_4}) or $X_{(HREE+Y)PO_4}$ components of monazite as determined by electron microprobe. (b–d) Tera–Wasserburg plots of uncorrected

monazite isotope ratios for Winchell Lake nappe samples EH30–EH31 (b), EH 45–EH49 (c), and EH48 (d) plotted with 2σ error ellipses. Interpreted growth domains correspond with numbers shown in parentheses in (a). Insets show full range of data with main plot area shown as black rectangle.

Figure 6. Zircon results from Winchell Lake nappe samples EH09–EH10. (a) Cathodoluminescence (CL) images of representative zircons showing SHRIMP analysis spot locations with ^{207}Pb-corrected ^{206}Pb/^{238}U ages and 2σ uncertainties. Left grain is from image shown in Fig 3b inset. (b) Tera–Wasserburg plot of uncorrected zircon isotope ratios (2σ uncertainty). See text for discussion.

Figure 7. Zircon results from Lizzies Basin block sample EH49. (a) Cathodoluminescence (CL) images of representative zircons showing SHRIMP analysis spot locations with ^{207}Pb-corrected ^{206}Pb/^{238}U ages and 2σ uncertainties. (b) Tera–Wasserburg plot of uncorrected zircon isotope ratios (2σ uncertainty). Inset shows full range of data with main plot area shown as black rectangle

Figure 8. Summary of U–Pb ages from monazite and zircon from the Winchell Lake nappe and Lizzies Basin block (this study). Vertical bars represent full age ranges, including 2σ uncertainties, of inferred growth zones. Vertical text adjacent to age ranges describes population: e.g. “mnz (1)” from sample EH30 is monazite population 1 (see Fig. 5a) and “mel.” zircon from sample EH49 is melanosome zircon.

Figure 9. Chondrite-normalized rare earth element abundance (“Coryell–Masuda”) diagrams (Coryell et al. 1963) for zircon and garnet from the East Humboldt Range. Plots were constructed using chondrite abundances from Anders and Grevesse (1989) multiplied by 1.3596 to maintain consistency with older literature. (a–c) Plots for zircon with gray region indicating

full range for comparison of zircon from the opposing crustal block (Winchell Lake nappe vs. Lizzies Basin block) of the East Humboldt Range. Dashed line symbols are the two oldest zircon grains referred to in the text. (d) Y Lα X-ray map of representative Winchell Lake nappe garnet (sample EH09) showing analyzed trace element spots. (e–g) Plots for melanosome garnet. Missing segments are elements that were below the detection limit for LA-ICPMS.

Figure 10. Ti–in–zircon thermometry results calculated for 3 East Humboldt Range samples. Individual boxes represent 1σ uncertainty in age and T calculations for $0.6 \leq a_{TiO2} \leq 1.0$ plus analytical uncertainty.

Figure 11. Equilibrium assemblage diagrams in the MnNCKFMASH+Y+P+Ce+F (F=fluid) system based on the general bulk composition SiO_2 = 54.486, Al_2O_3 = 20.073, MgO = 3.004, FeO = 9.866, MnO = 0.397, CaO = 1.043, Na_2O = 0.658, K_2O = 5.687, H_2O = 4.384, F = 0.019, P = 0.306, Y = 0.008, Ce_2O_3 = 0.069, which is similar to that of Winchell Lake nappe samples EH09–EH10. Modified from Spear and Pyle (2010). Excess H_2O is removed just below the solidus. Proposed P–T path for the Winchell Lake nappe is shown as thick black path, as in Hallett and Spear (2014). (a) Light gray lines are molar isopleths of garnet (mmol per 100 g of rock), roughly 0.32 x volume % (Spear and Pyle 2010). Xenotime-bearing assemblages are not shown for simplicity. (b-d) Stable assemblages as in (a). Dashed dark gray line is xenotime-out based on the interpretation that the rocks had a relatively low effective Y content in the bulk composition due to Y sequestration in garnet cores. (b) Light gray lines are X_{YAG} per mil. (c) Light gray lines are molar isopleths of monazite (mmol per 100 g of rock), roughly 0.12 x volume % (Spear and Pyle 2010). Circled numbers correspond to monazite compositional/age zones in Fig. 4a and text. (d) Light gray lines are X_{YPO_4} in monazite. Inset shows alternative

interpretation for monazite (3) including Eocene–Oligocene heating into a xenotime stable assemblage.

Figure 12. Retrograde reaction textures. Abbreviations are lower case versions of Kretz (1983). (a) Transmitted light image of resorbed garnet from Winchell Lake nappe sample EH10. (b) Sketch of (a), see text for interpretation.

Figure 13. Interpretive P–T–t paths for the northern East Humboldt Range. Solidus estimates are from Hallett and Spear (2014). Dashed portions of paths are not well constrained by relict assemblages. Age ranges given are approximated by 1σ envelopes for probability densities of ranges given in the text. (a) Winchell Lake nappe (WLN), includes geothermochronologic constraints from monazite and zircon. EH21 monazite inclusion in garnet ages are not shown. (b) Lizzies Basin block (LBB), showing possible reheating/melt flux event in Latest Cretaceous–Paleocene time. Spread monazite (2) ages from EH30–EH31 is not shown. Possible Eocene–Oligocene reheating/fluid event also shown, as in (a).

DESCRIPTION OF SUPPLEMENTARY MATERIAL

1. Supplementary.xls: The following spreadsheet data tables are included.

- ZrnTE–SHRIMP: Trace elements in zircon
- ZirconUPbSHRIMP: U/Th–Pb zircon SHRIMP data
- MonaziteEMP: Electron microprobe monazite results
- MonaziteSHRIMP: Monazite U/Th–Pb and trace element SHRIMP data
- GrtTE: LA–ICPMS Trace elements in garnet
- ApatiteEMP: Electron microprobe major elements in apatite
- MnzProbeSettings: Electron microprobe settings for monazite analyses

1345 2. Detailed_Analytical_Methods.doc

1346 3. EH09_leucosome grt REE.pdf

1347 4. Spot_Locations.pdf: Zircon and monazite images showing SHRIMP and EMP analysis

1348 locations.

Table 1: Monazite, xenotime, and garnet thermometry results.

Sample	Mnz X_{Y+HREE}	Mnz zone	n (Mnz)	Mnz+Xno*	ppm Y grt	Grt zone	YAG+Xno†	X_{Ca} grt	XAn	X_{YPO4} Mnz	X_{YAG}	X_{OH} Ap	fH_2O‡	ln K_{eq}	YAG+Mnz*
EH09	0.0223	1 (core)	7	363 ± 38 ºC	–	–	–	–	–	–	–	–	–	–	–
	–	–	–	–	4200	core§	470 ± 7 ºC	–	–	–	–	–	–	–	–
	–	2 (mant)	9	–	469	rim	–	0.0645	0.44	0.0220	0.00087	0.043	4250	12.555	678 ± 19 ºC
	0.0724	3 (rim)	6	525 ± 47 ºC	–	–	–	–	–	–	–	–	–	–	–
EH10	0.0248	1 (core)	11	437 ± 14 ºC	–	–	–	–	–	–	–	–	–	–	–
	–	–	–	–	1900	core§	498 ± 3 ºC	–	–	–	–	–	–	–	–
	–	2 (mant)	7	–	497	rim	–	0.0780	0.47	0.0264	0.00101	0.027	4400	13.483	694 ± 21 ºC
	0.0804	3 (rim)	8	558 ± 28 ºC	–	–	–	–	–	–	–	–	–	–	–
EH49	0.0550	2 (core)	3	445 ± 28 ºC	–	–	–	–	–	–	–	–	–	–	–
	–	–	–	–	305	core§	564 ± 7 ºC	–	–	–	–	–	–	–	–
	–	3 (mant)	3	–	106	rim	–	0.038	0.20	0.0188	0.00026	0.141	4192	12.250	672 ± 25 ºC
	0.0727	4 (rim)	4	529 ± 21 ºC‖	–	rim	–	–	–	–	–	–	–	–	–

* Calibration of Pyle et al. (2001), P = 5.5 kbar for YAG + monazite thermometry.
† Calibration of Pyle and Spear (2000), accuracy estimated at ± 30º C.
‡ Calculated at P and T using methods of Pitzer and Sterner (1994) and Sterner and Pitzer (1994).
§ No monazite is interpreted to be in equilibrium with garnet cores.
‖ The age of this monazite is poorly constrained, and may be Cretaceous or Eocene–Oligocene.

Table 2: Burial and Exhumation Rates

	upper constraint	lower constraint	age from (Ma)	age to (Ma)	Duration (m.y.)	∆kbar	kbar/m.y.	km/m.y.
WLN upper limb burial max	1σ within EH09–10 mnz (1)	1σ within EH09–10 zircon range	82.1	77.1	5	7	1.4	4.6
WLN upper limb burial min	1σ within EH09–10 mnz (1)	1σ within EH09–10 zircon range	83.5	62.4	21.1	7	0.3	1.1
WLN upper limb exhumation max	1σ within EH09–10 mnz (1)	1σ within EH09–10 zircon range	82.1	77.1	5	3	0.6	2.0
WLN upper limb exhumation min	1σ within EH09–10 mnz (1)	1σ within EH09–10 zircon range	83.5	62.4	21.1	3	0.1	0.5
LBB burial max	1σ within EH45–49 mnz (2)	1σ within EH48 monazite	86.8	80.8	6	3	0.5	1.7
LBB burial min	1σ within EH45–49 mnz (2)	1σ within EH48 monazite	97.5	79.4	18.1	3	0.2	0.5
LBB exhumation max	1σ within EH45–49 mnz (2)	1σ within EH48 monazite	86.8	80.8	6	2	0.3	1.1
LBB exhumation min	1σ within EH45–49 mnz (2)	1σ within EH48 monazite	97.5	79.4	18.1	2	0.1	0.4

Note: Age constraints that correspond to ranges given in the text are approximated by 1σ envelopes for probability densities calculated for ^{207}Pb corrected $^{206}Pb/^{238}U$ ages.

Table 3: Heating and Cooling Rates

	upper constraint	lower constraint	age from (Ma)	age to (Ma)	Duration (m.y.)	ΔT	ºC/m.y.
WLN upper limb heating max	1σ within EH09–10 mnz (1)	1σ within EH09–10 zrn range	82.1	77.1	5	300	60.0
WLN upper limb heating min	1σ within EH09–10 mnz (1)	1σ within EH09–10 zrn range	83.5	62.4	21.1	300	14.2
WLN upper limb cooling max	1σ within EH09–10 zircon range	1σ within EH09–10 mnz (3)	62.4	40	22.4	200	8.9
WLN upper limb cooling min	1σ within EH09–10 zircon range	1σ within EH09–10 mnz (3)	77.1	32	45.1	200	4.4
LBB heating max	1σ within EH45–49 mnz (2)	1σ within EH48 monazite	86.8	80.8	6	300	33.3
LBB heating min	1σ within EH45–49 mnz (2)	1σ within EH48 monazite	97.5	79.4	18.1	300	11.0

Note: Age constraints that correspond to ranges given in the text are approximated by 1σ envelopes for probability densities calculated for ^{207}Pb corrected $^{206}Pb/^{238}U$ ages.

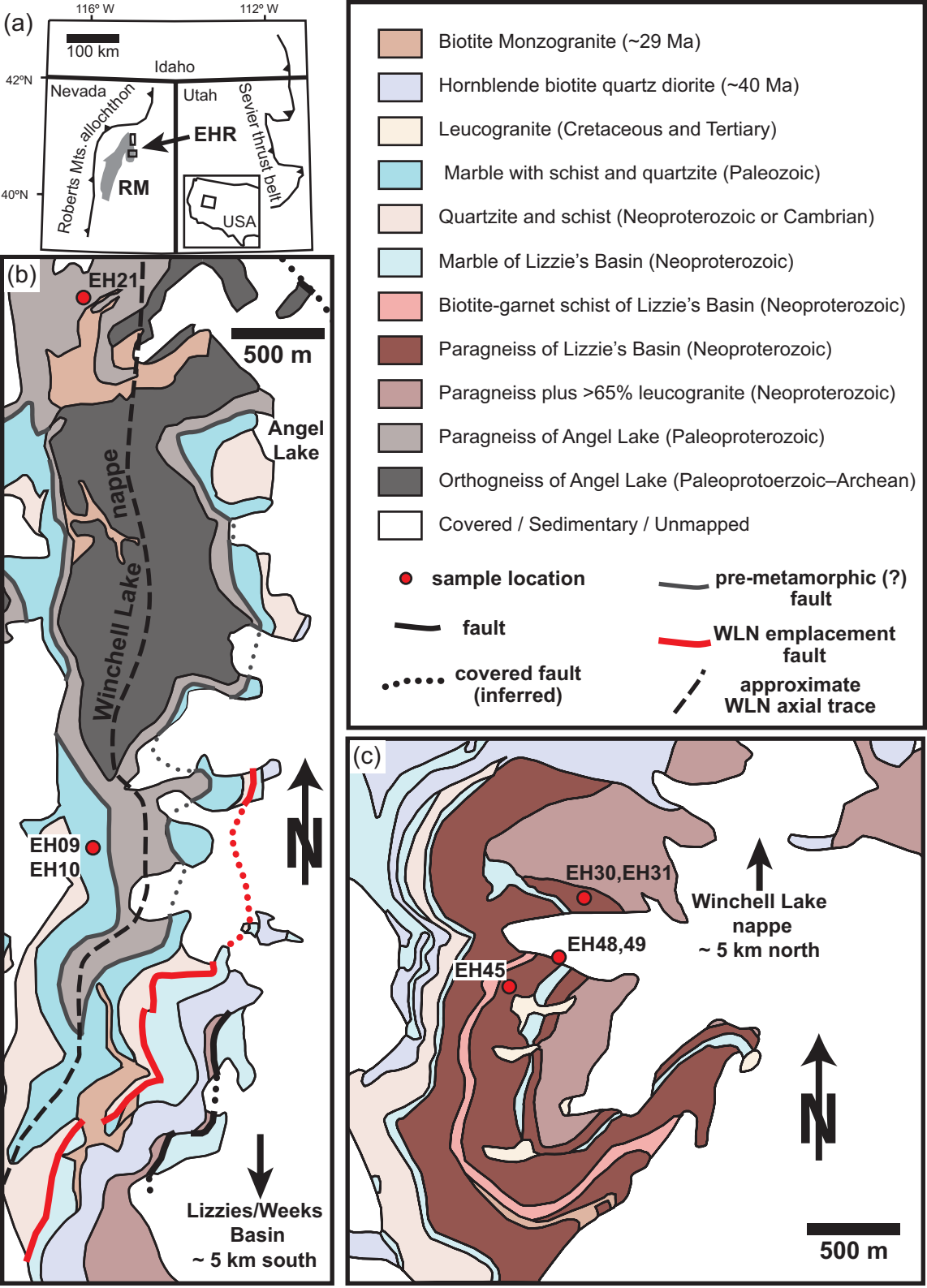
(a)
116° W
112° W
100 km
Idaho
42°N
Nevada
Utah
Roberts Mts. allochthon
Sevier thrust belt
EHR
RM
40°N
USA
(b)
EH21
500 m
Angel Lake
Winchell Lake nappe
EH09
EH10
N
Lizzies/Weeks Basin
~ 5 km south
Biotite Monzogranite (~29 Ma)
Hornblende biotite quartz diorite (~40 Ma)
Leucogranite (Cretaceous and Tertiary)
Marble with schist and quartzite (Paleozoic)
Quartzite and schist (Neoproterozoic or Cambrian)
Marble of Lizzie's Basin (Neoproterozoic)
Biotite-garnet schist of Lizzie's Basin (Neoproterozoic)
Paragneiss of Lizzie's Basin (Neoproterozoic)
Paragneiss plus >65% leucogranite (Neoproterozoic)
Paragneiss of Angel Lake (Paleoproterozoic)
Orthogneiss of Angel Lake (Paleoprotoerzoic–Archean)
Covered / Sedimentary / Unmapped
sample location
fault
covered fault (inferred)
pre-metamorphic (?) fault
WLN emplacement fault
approximate WLN axial trace
(c)
EH30,EH31
Winchell Lake nappe
~ 5 km north
EH48,49
EH45
N
500 m

Figure 1

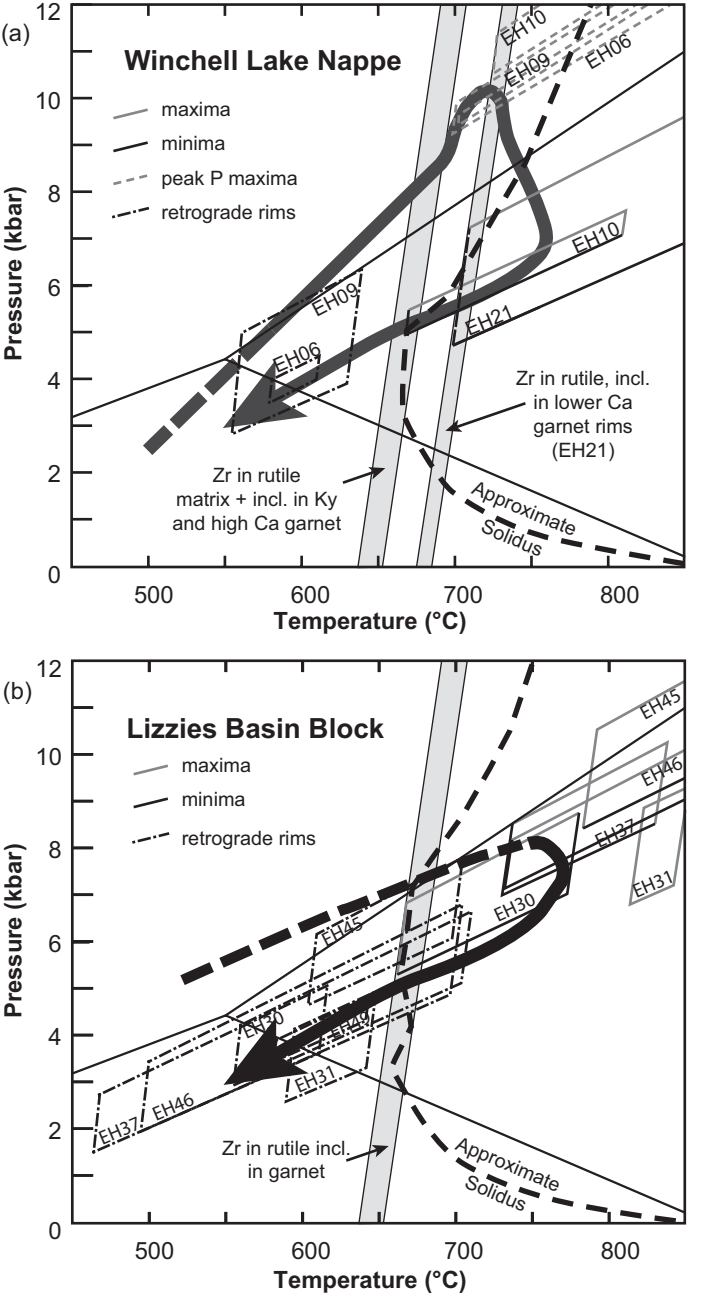
(a)
Winchell Lake Nappe
maxima
minima
peak P maxima
retrograde rims
EH10
EH09
EH06
EH10
EH09
EH21
EH06
Zr in rutile, incl.
in lower Ca
garnet rims
(EH21)
Zr in rutile
matrix + incl. in Ky
and high Ca garnet
Approximate
Solidus
Pressure (kbar)
Temperature (°C)
(b)
Lizzies Basin Block
maxima
minima
retrograde rims
EH45
EH46
EH37
EH31
EH30
EH45
EH30
EH31
EH37
EH46
Zr in rutile incl.
in garnet
Approximate
Solidus
Pressure (kbar)
Temperature (°C)

Figure 2

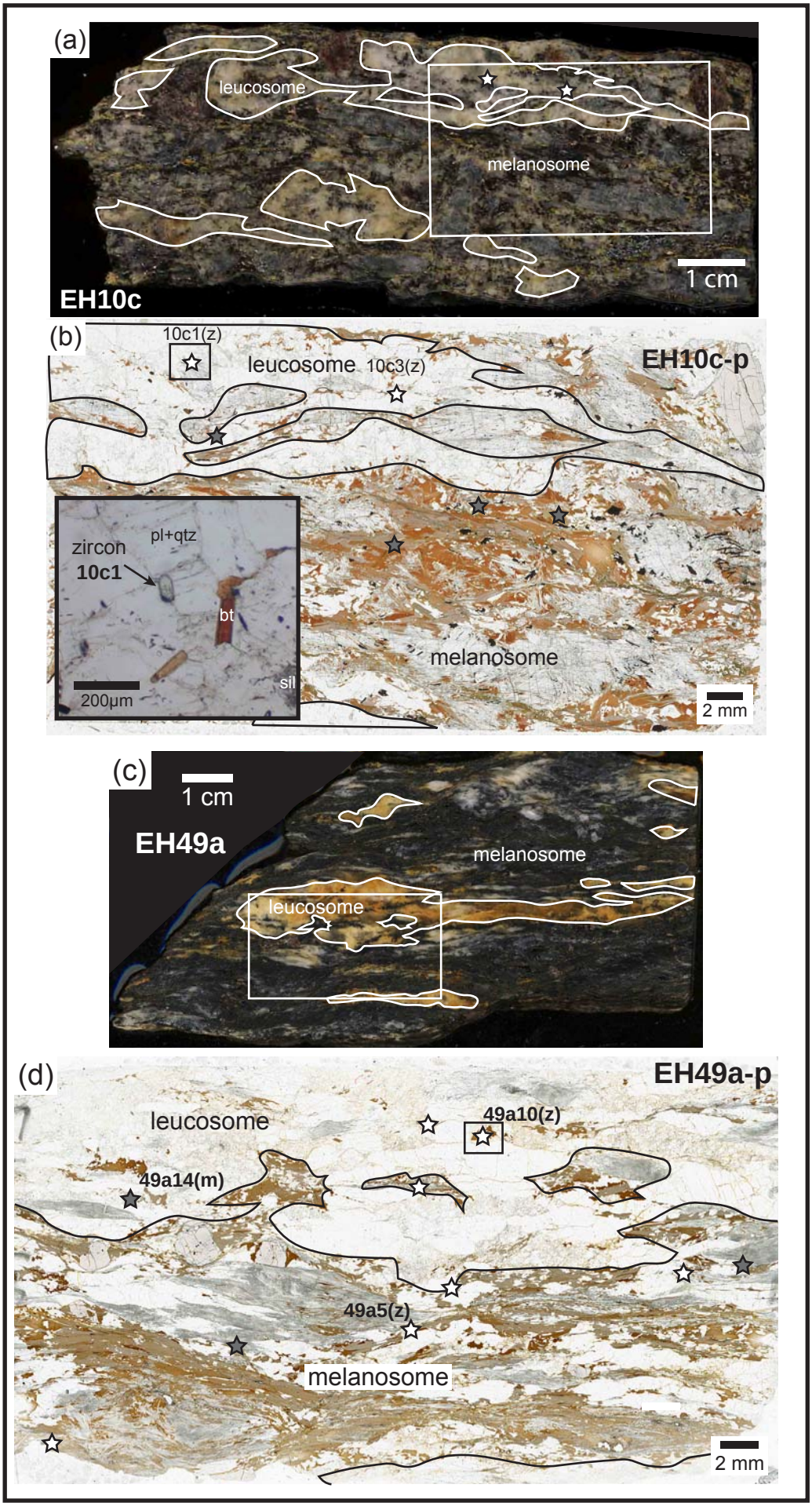
(a)
leucosome
melanosome
1 cm
EH10c
(b)
10c1(z)
leucosome
10c3(z)
EH10c-p
zircon
10c1
pl+qtz
bt
sil
200µm
melanosome
2 mm
(c)
1 cm
EH49a
melanosome
leucosome
(d)
EH49a-p
leucosome
49a10(z)
49a14(m)
49a5(z)
melanosome
2 mm

Figure 3

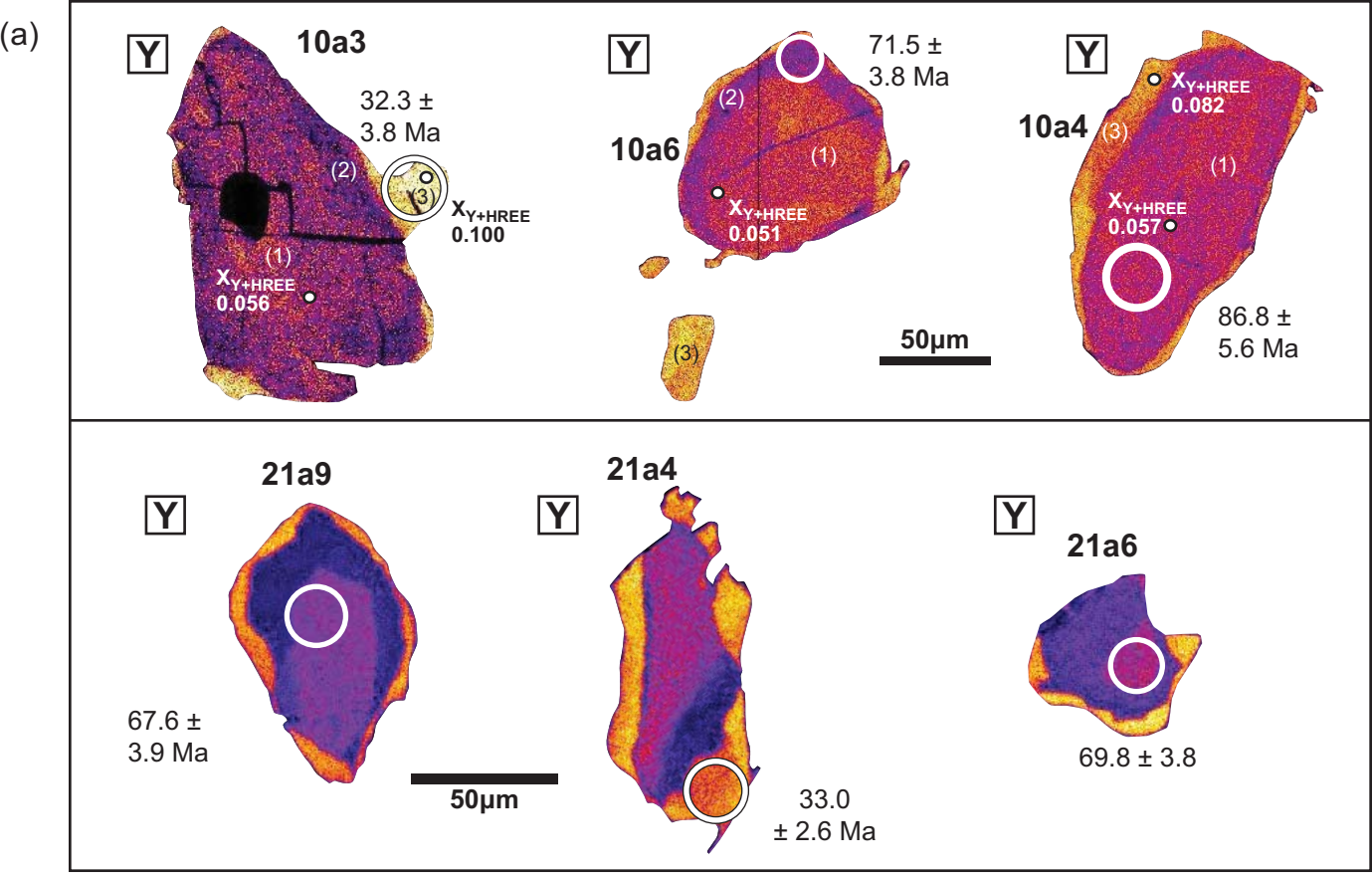
(a)
Y
10a3
32.3 ± 3.8 Ma
(2)
(3)
X_{Y+HREE} 0.100
(1)
X_{Y+HREE} 0.056
Y
71.5 ± 3.8 Ma
10a6
(2)
(1)
X_{Y+HREE} 0.051
(3)
50µm
Y
X_{Y+HREE} 0.082
10a4
(3)
(1)
X_{Y+HREE} 0.057
86.8 ± 5.6 Ma
Y
21a9
67.6 ± 3.9 Ma
50µm
Y
21a4
33.0 ± 2.6 Ma
Y
21a6
69.8 ± 3.8

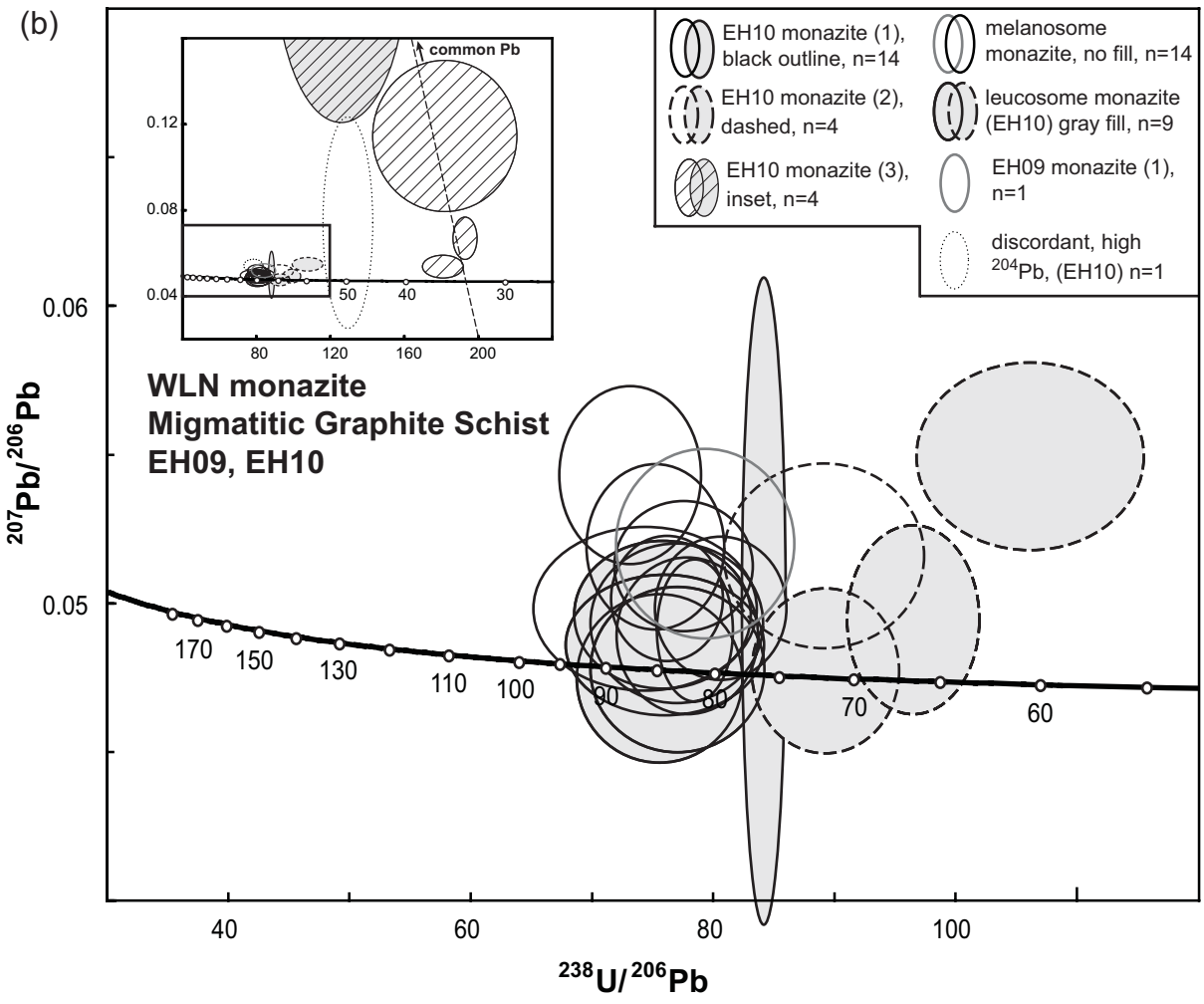
(b)
common Pb
0.12
0.08
0.04
50
40
30
80
120
160
200
EH10 monazite (1), black outline, n=14
EH10 monazite (2), dashed, n=4
EH10 monazite (3), inset, n=4
melanosome monazite, no fill, n=14
leucosome monazite (EH10) gray fill, n=9
EH09 monazite (1), n=1
discordant, high ^{204}Pb, (EH10) n=1
WLN monazite
Migmatitic Graphite Schist
EH09, EH10
0.06
0.05
170
150
130
110
100
90
80
70
60
40
60
80
100
^{207}Pb/^{206}Pb
^{238}U/^{206}Pb

Figure 4a,b

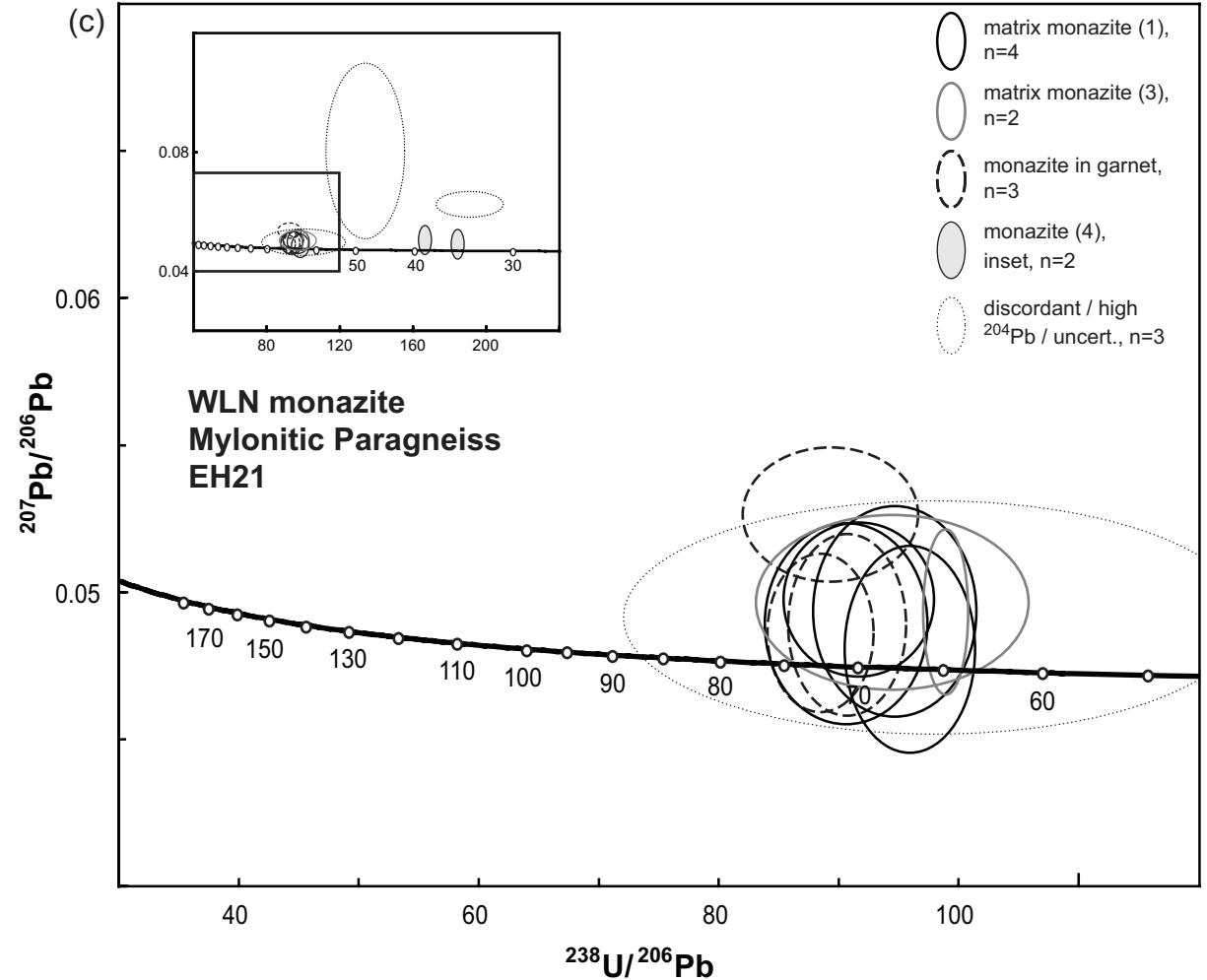
(c)
matrix monazite (1), n=4
matrix monazite (3), n=2
monazite in garnet, n=3
monazite (4), inset, n=2
discordant / high 204Pb / uncert., n=3
WLN monazite
Mylonitic Paragneiss
EH21
0.08
0.04
80
120
160
200
50
40
30
0.06
0.05
170
150
130
110
100
90
80
70
60
40
60
80
100
207Pb/206Pb
238U/206Pb

Figure 4c

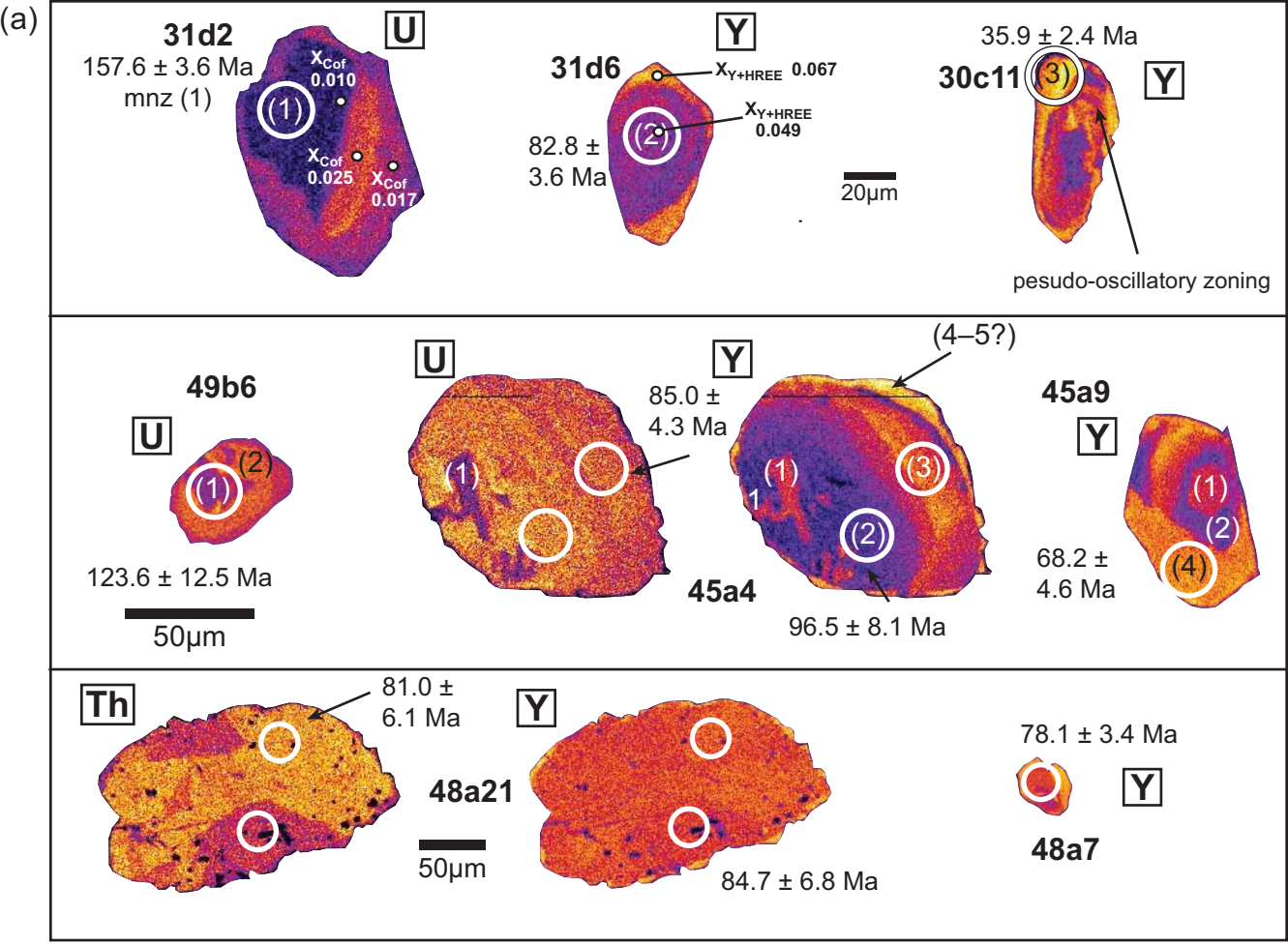
(a)
31d2
157.6 ± 3.6 Ma
mnz (1)
U
(1)
X_{Cof} 0.010
X_{Cof} 0.025
X_{Cof} 0.017
31d6
Y
X_{Y+HREE} 0.067
X_{Y+HREE} 0.049
82.8 ± 3.6 Ma
(2)
20μm
35.9 ± 2.4 Ma
30c11
(3)
Y
pesudo-oscillatory zoning
49b6
U
(1)
(2)
123.6 ± 12.5 Ma
50μm
U
(1)
85.0 ± 4.3 Ma
Y
(4–5?)
(1)
(2)
(3)
45a4
96.5 ± 8.1 Ma
45a9
Y
(1)
(2)
(4)
68.2 ± 4.6 Ma
Th
81.0 ± 6.1 Ma
48a21
50μm
Y
84.7 ± 6.8 Ma
78.1 ± 3.4 Ma
Y
48a7

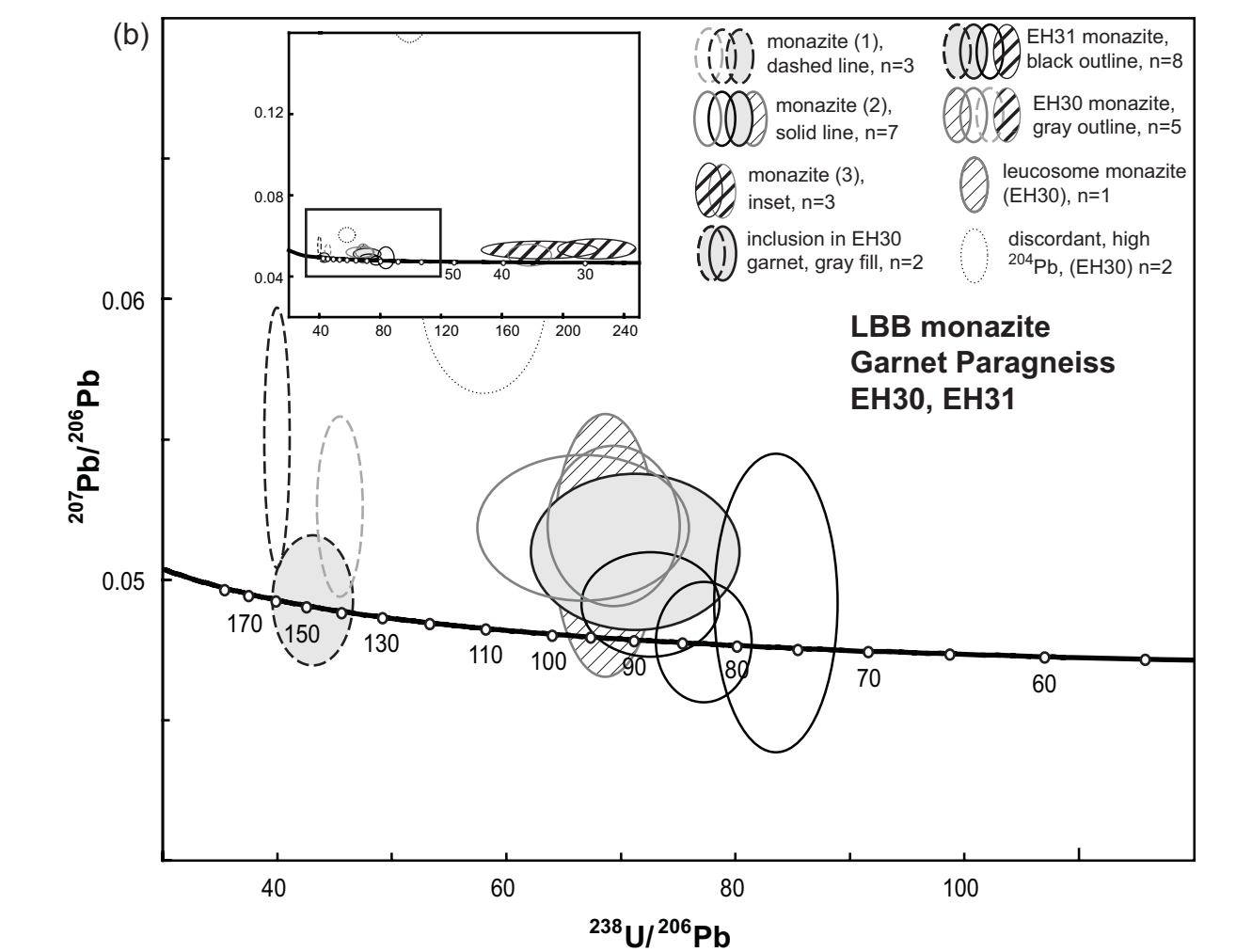
(b)
monazite (1), dashed line, n=3
monazite (2), solid line, n=7
monazite (3), inset, n=3
inclusion in EH30 garnet, gray fill, n=2
EH31 monazite, black outline, n=8
EH30 monazite, gray outline, n=5
leucosome monazite (EH30), n=1
discordant, high ^{204}Pb, (EH30) n=2
LBB monazite
Garnet Paragneiss
EH30, EH31
^{207}Pb/^{206}Pb
^{238}U/^{206}Pb
0.12
0.08
0.04
0.06
0.05
40
80
120
160
200
240
50
40
30
170
150
130
110
100
90
80
70
60
40
60
80
100

Figure 5a,b

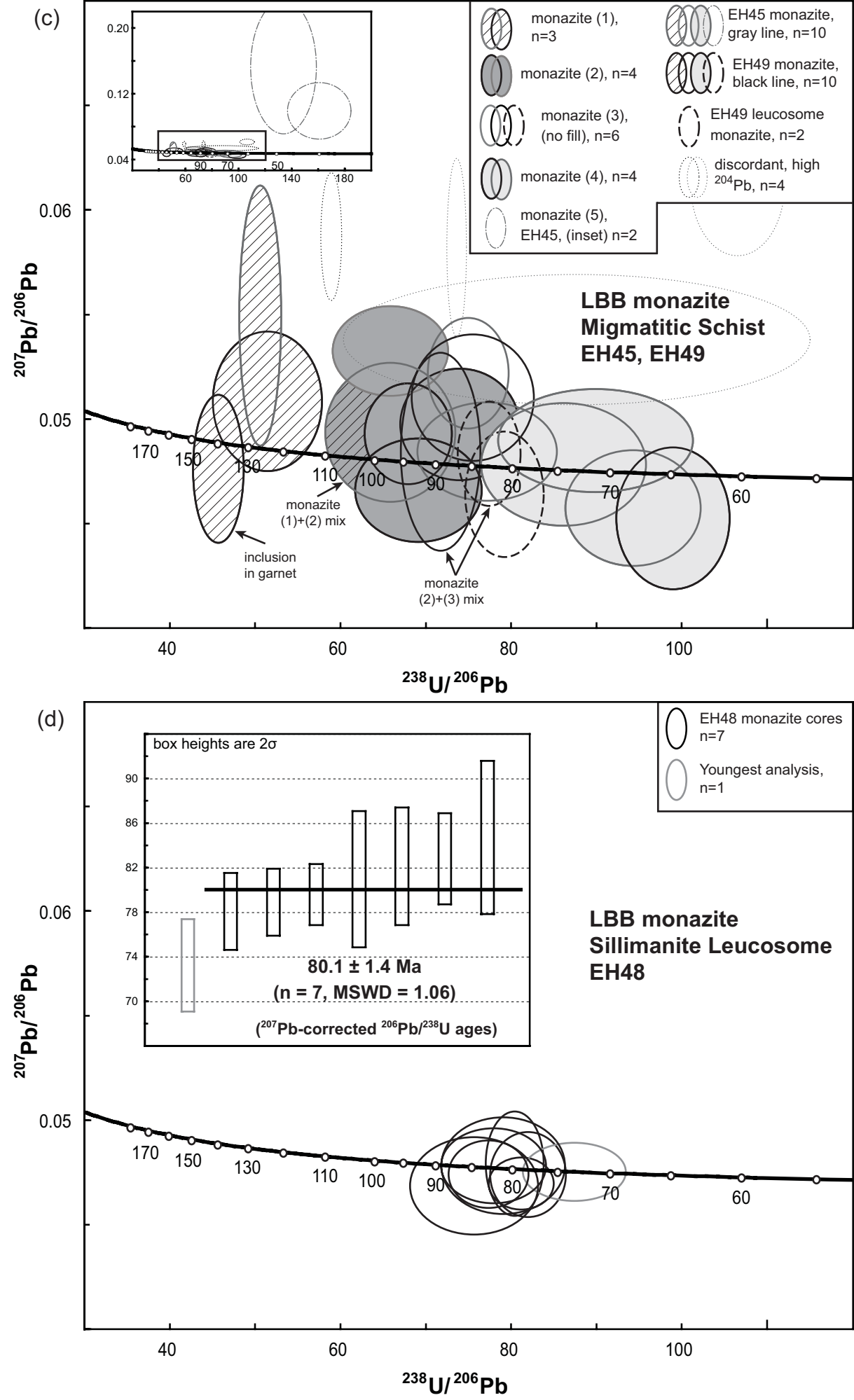
(c)
monazite (1), n=3
monazite (2), n=4
monazite (3), (no fill), n=6
monazite (4), n=4
monazite (5), EH45, (inset) n=2
EH45 monazite, gray line, n=10
EH49 monazite, black line, n=10
EH49 leucosome monazite, n=2
discordant, high 204Pb, n=4
LBB monazite
Migmatitic Schist
EH45, EH49
inclusion in garnet
monazite (1)+(2) mix
monazite (2)+(3) mix
207Pb/206Pb
238U/206Pb
(d)
box heights are 2σ
EH48 monazite cores n=7
Youngest analysis, n=1
80.1 ± 1.4 Ma
(n = 7, MSWD = 1.06)
(207Pb-corrected 206Pb/238U ages)
LBB monazite
Sillimanite Leucosome
EH48

Figure 5c,d

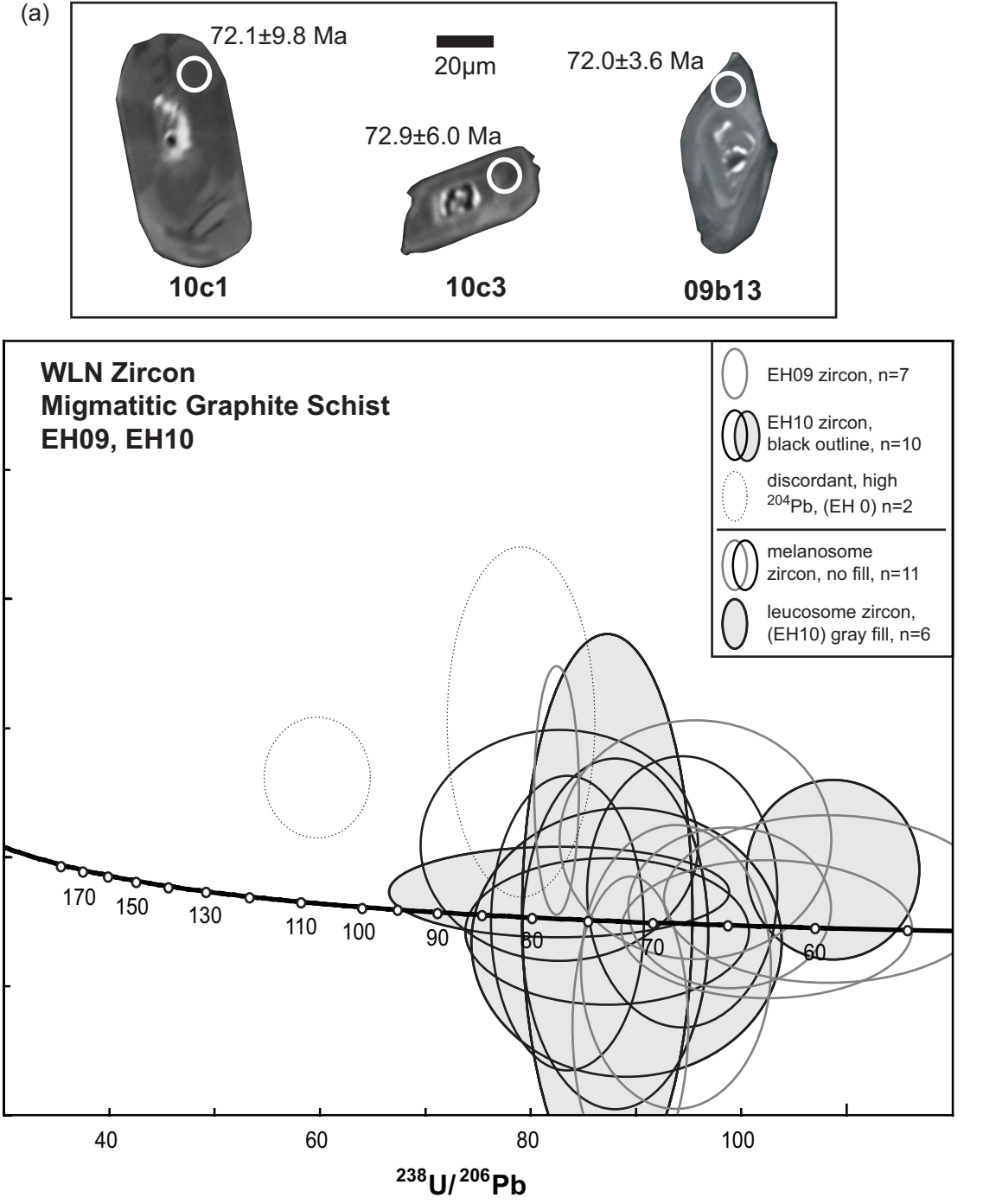
(a)
72.1±9.8 Ma
20μm
72.0±3.6 Ma
72.9±6.0 Ma
10c1
10c3
09b13
(b)
WLN Zircon
Migmatitic Graphite Schist
EH09, EH10
EH09 zircon, n=7
EH10 zircon, black outline, n=10
discordant, high 204Pb, (EH 0) n=2
melanosome zircon, no fill, n=11
leucosome zircon, (EH10) gray fill, n=6
0.06
0.05
207Pb/206Pb
170
150
130
110
100
90
80
70
60
40
60
80
100
238U/206Pb

Figure 6

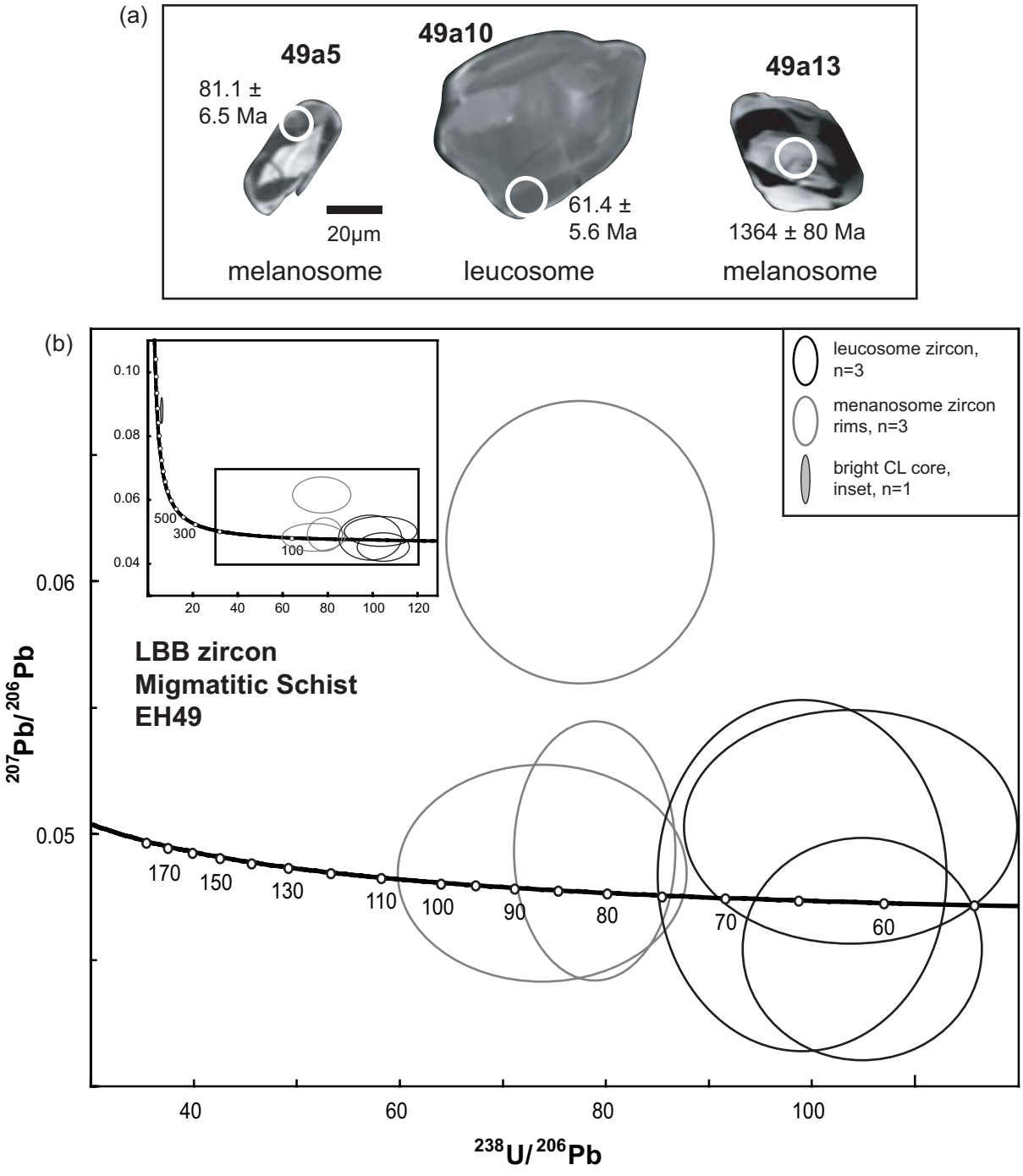
(a)
49a5
81.1 ±
6.5 Ma
20μm
melanosome
49a10
61.4 ±
5.6 Ma
leucosome
49a13
1364 ± 80 Ma
melanosome
(b)
leucosome zircon, n=3
menanosome zircon rims, n=3
bright CL core, inset, n=1
LBB zircon
Migmatitic Schist
EH49
207Pb/206Pb
238U/206Pb
0.06
0.05
40
60
80
100
170
150
130
110
100
90
80
70
60
0.10
0.08
0.06
0.04
500
300
100
20
40
60
80
100
120

Figure 7

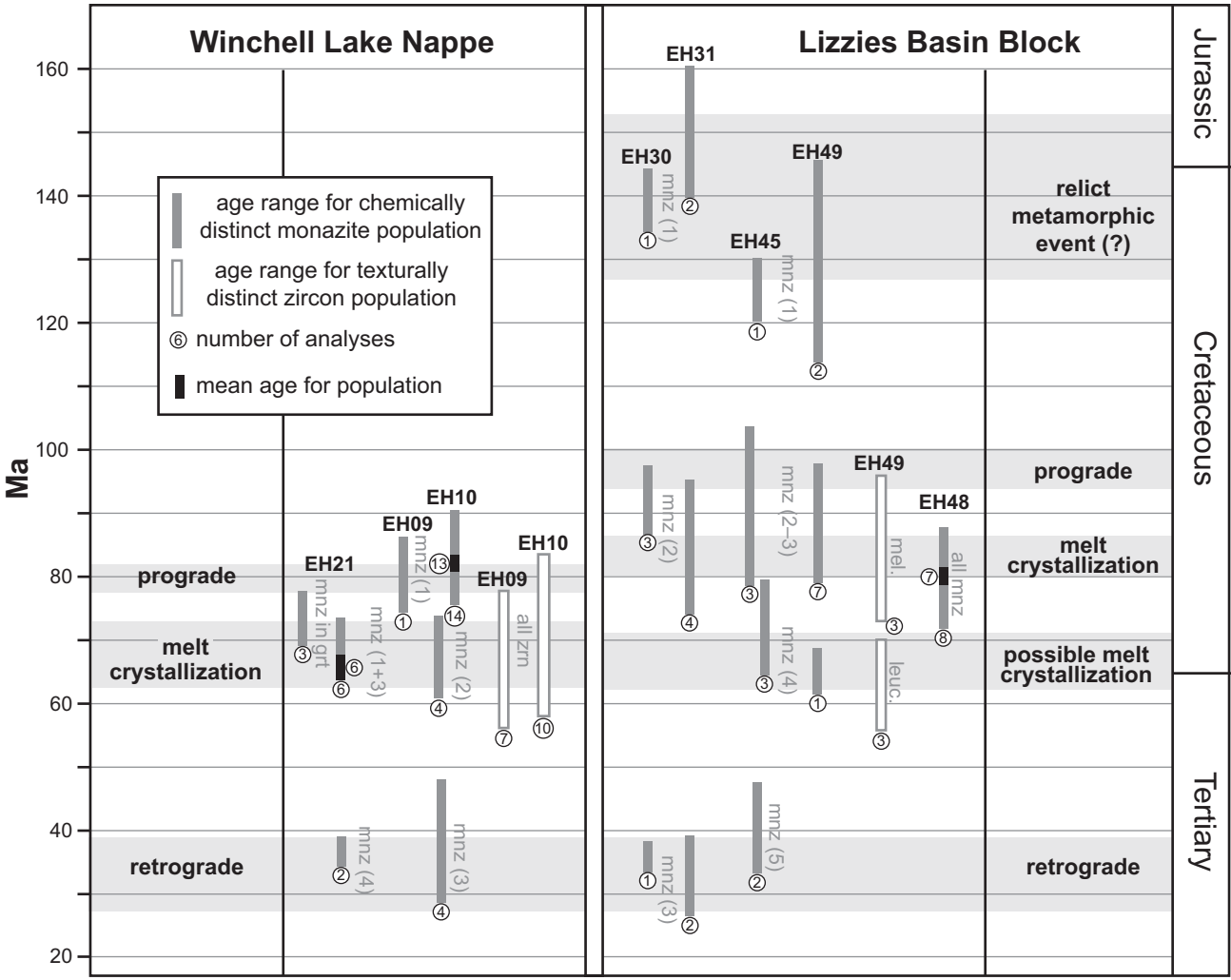
Winchell Lake Nappe
Lizzies Basin Block
Ma
160
140
120
100
80
60
40
20
age range for chemically distinct monazite population
age range for texturally distinct zircon population
⑥ number of analyses
mean age for population
prograde
melt crystallization
retrograde
EH21
mnz in grt
mnz (1+3)
EH09
mnz (1)
EH10
mnz (2)
EH09
all zrn
EH10
mnz (4)
mnz (3)
EH31
EH30
mnz (1)
EH45
mnz (1)
EH49
mnz (2–3)
mnz (2)
mnz (4)
EH49
mel.
leuc.
EH48
all mnz
mnz (5)
mnz (3)
relict metamorphic event (?)
prograde
melt crystallization
possible melt crystallization
retrograde
Jurassic
Cretaceous
Tertiary

Figure 8

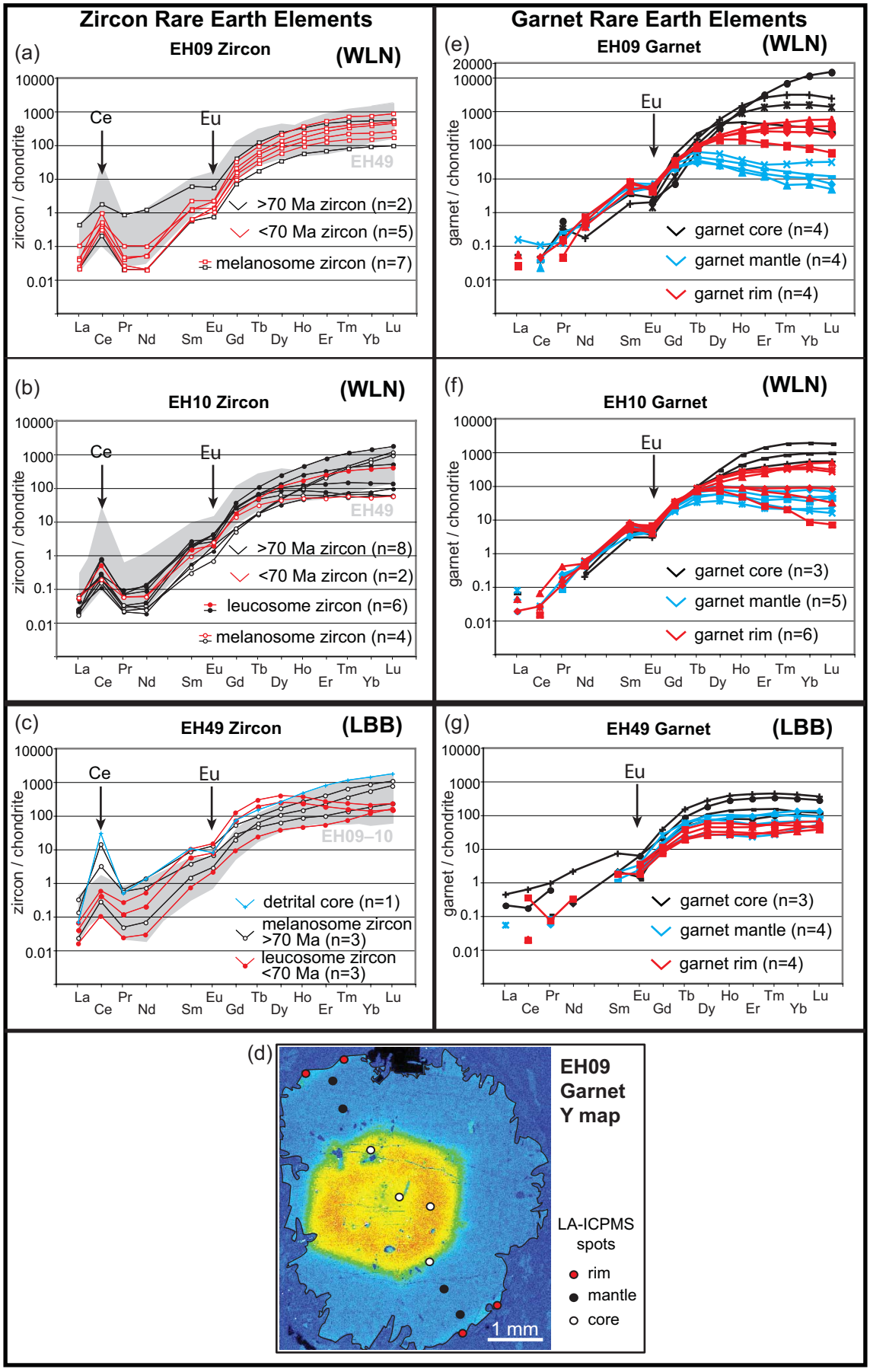
Zircon Rare Earth Elements
(a)
EH09 Zircon
(WLN)
zircon / chondrite
Ce
Eu
EH49
>70 Ma zircon (n=2)
<70 Ma zircon (n=5)
melanosome zircon (n=7)
(b)
EH10 Zircon
(WLN)
>70 Ma zircon (n=8)
<70 Ma zircon (n=2)
leucosome zircon (n=6)
melanosome zircon (n=4)
(c)
EH49 Zircon
(LBB)
EH09–10
detrital core (n=1)
melanosome zircon >70 Ma (n=3)
leucosome zircon <70 Ma (n=3)
La Ce Pr Nd Sm Eu Gd Tb Dy Ho Er Tm Yb Lu
Garnet Rare Earth Elements
(e)
EH09 Garnet
(WLN)
garnet / chondrite
Eu
garnet core (n=4)
garnet mantle (n=4)
garnet rim (n=4)
(f)
EH10 Garnet
(WLN)
garnet core (n=3)
garnet mantle (n=5)
garnet rim (n=6)
(g)
EH49 Garnet
(LBB)
garnet core (n=3)
garnet mantle (n=4)
garnet rim (n=4)
(d)
EH09 Garnet Y map
LA-ICPMS spots
rim
mantle
core
1 mm

Figure 9

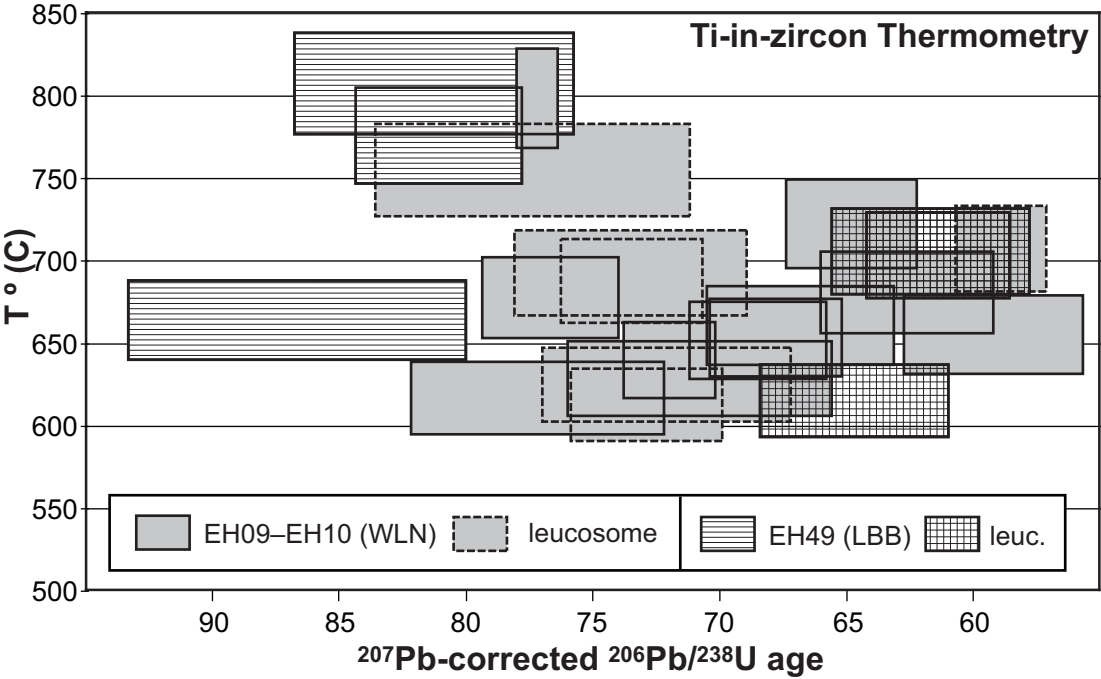
Ti-in-zircon Thermometry
T ° (C)
850
800
750
700
650
600
550
500
90
85
80
75
70
65
60
207Pb-corrected 206Pb/238U age
EH09–EH10 (WLN)
leucosome
EH49 (LBB)
leuc.

Figure 10

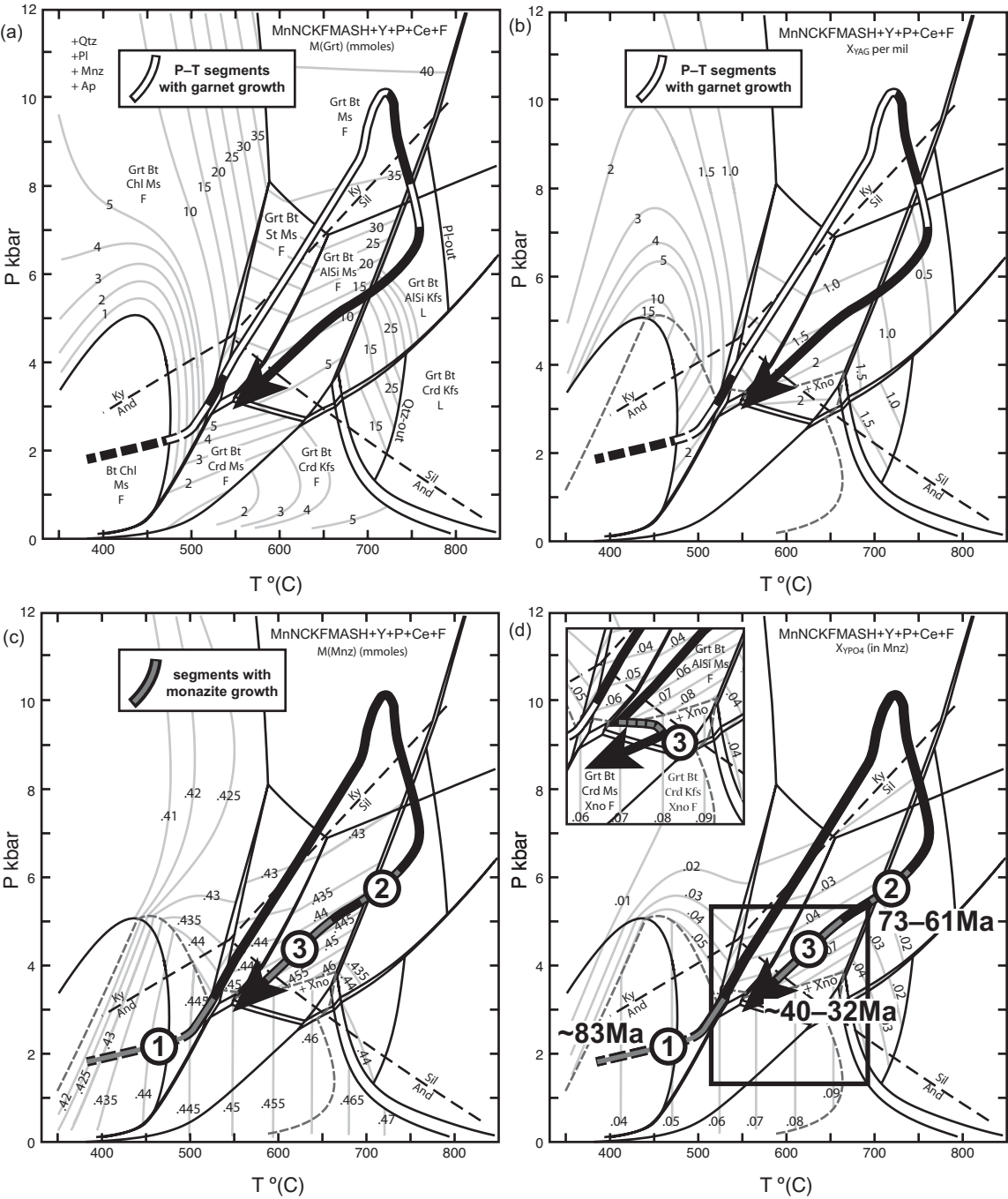
(a)
MnNCKFMASH+Y+P+Ce+F
M(Grt) (mmoles)
+Qtz
+Pl
+ Mnz
+ Ap
P–T segments with garnet growth
Grt Bt Ms F
Grt Bt Chl Ms F
Grt Bt St Ms F
Grt Bt AlSi Ms F
Grt Bt AlSi Kfs L
Grt Bt Crd Kfs L
Grt Bt Crd Ms F
Grt Bt Crd Kfs F
Bt Chl Ms F
Pl-out
Qtz-out
Ky
Sil
And
P kbar
T °(C)
(b)
MnNCKFMASH+Y+P+Ce+F
XYAG per mil
P–T segments with garnet growth
Xno
(c)
MnNCKFMASH+Y+P+Ce+F
M(Mnz) (mmoles)
segments with monazite growth
(d)
MnNCKFMASH+Y+P+Ce+F
XYPO4 (in Mnz)
Grt Bt AlSi Ms F
Grt Bt Crd Ms Xno F
Grt Bt Crd Kfs Xno F
73–61Ma
~40–32Ma
~83Ma

Figure 11

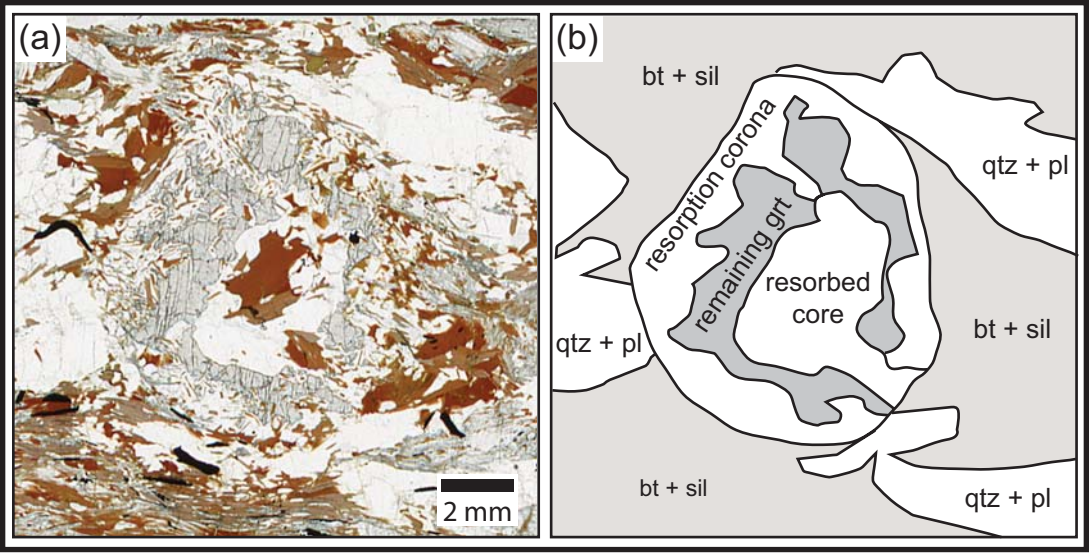
(a)
2 mm
(b)
bt + sil
resorption corona
qtz + pl
remaining grt
resorbed
core
qtz + pl
bt + sil
bt + sil
qtz + pl

Figure 12

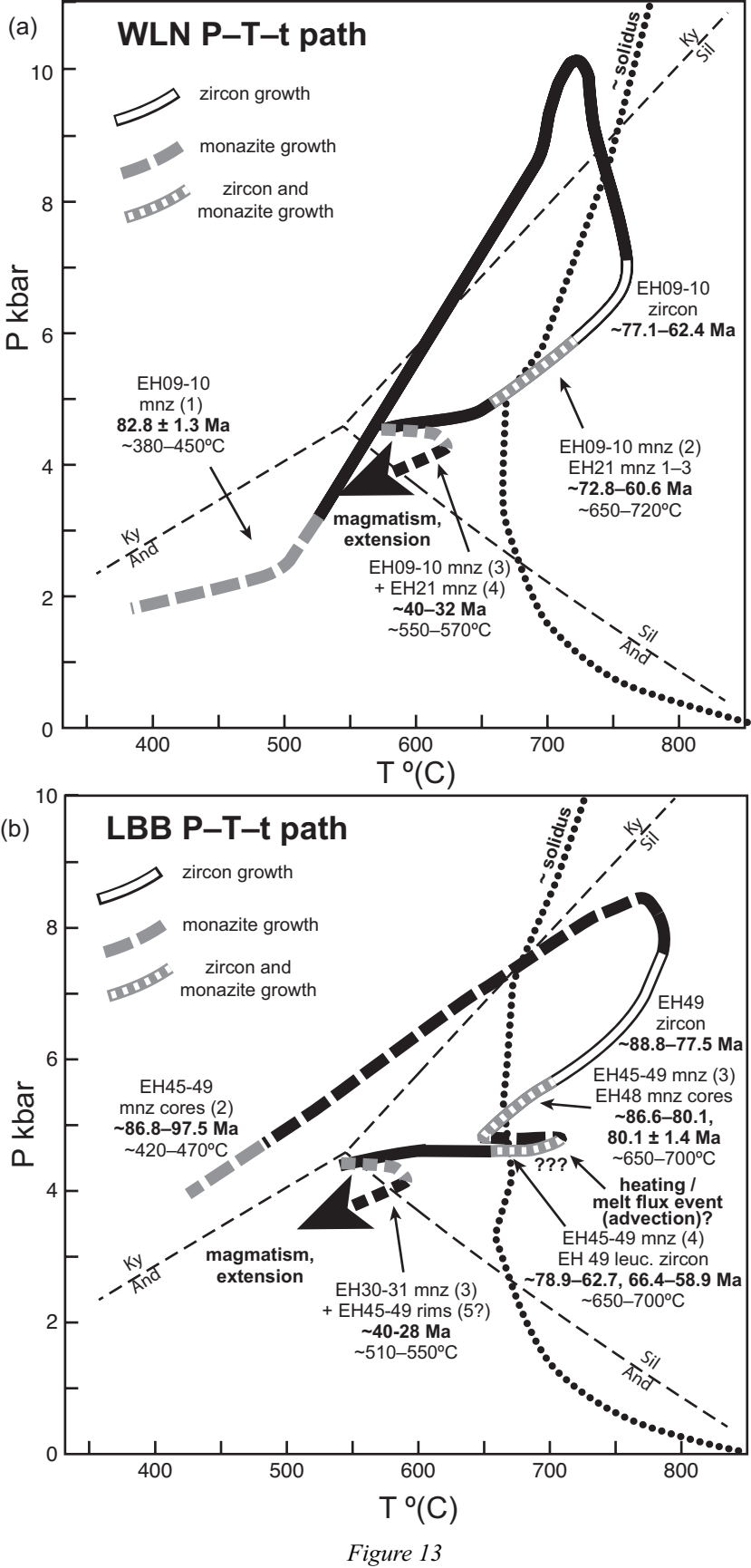
(a)
WLN P–T–t path
zircon growth
monazite growth
zircon and monazite growth
~ solidus
Ky
Sil
EH09-10 zircon ~77.1–62.4 Ma
EH09-10 mnz (1) 82.8 ± 1.3 Ma ~380–450ºC
EH09-10 mnz (2) EH21 mnz 1–3 ~72.8–60.6 Ma ~650–720ºC
magmatism, extension
EH09-10 mnz (3) + EH21 mnz (4) ~40–32 Ma ~550–570ºC
Ky And
Sil And
P kbar
T ºC
(b)
LBB P–T–t path
zircon growth
monazite growth
zircon and monazite growth
~ solidus
Ky
Sil
EH49 zircon ~88.8–77.5 Ma
EH45-49 mnz cores (2) ~86.8–97.5 Ma ~420–470ºC
EH45-49 mnz (3) EH48 mnz cores ~86.6–80.1, 80.1 ± 1.4 Ma ~650–700ºC
???
heating / melt flux event (advection)?
EH45-49 mnz (4) EH 49 leuc. zircon ~78.9–62.7, 66.4–58.9 Ma ~650–700ºC
magmatism, extension
EH30-31 mnz (3) + EH45-49 rims (5?) ~40-28 Ma ~510–550ºC
Ky And
Sil And
P kbar
T ºC

Figure 13